# ATLAS NOTE

ATL-ATL-INDET-PUB-2007-xxx, V1.0

May 17, 2007

## Pixel Offline Analysis for EndcapA Cosmic Data

The ATLAS Pixel System Test Group

### Abstract

This document summarizes the results of the offline analysis for the pixel endcapA system test cosmic data. The setup consists of one pixel endcap of three disks, for a total of 144 modules and 6.6 million channels, about the 8% of the full detector with the goal of exercising the readout system, data taking and testing the offline reconstruction chain. The observed noise occupancy is found to be $10^{-9}$ after removing all the noisy pixels. Comparison with the detector characterization performed during the detector assembly shows that most of these noisy pixels were already flagged during the production test. The tracking studies, especially the ones related to particles passing in the overlap regions between adjacent modules, have been very useful in spotting problems in our geometry description and can be used for the relative alignment between the adjacent modules. When using the geometry taken from the detector survey, an initial resolution of 21.2 $\mu m$ is obtained. After a preliminary alignment this improves to 17.8 $\mu m$. The difference with the 15.8 $\mu m$ expected from MC simulation are probably due to residual alignment uncertainties which are under investigation.

# 1 Introduction

In December 2006 an endcap of the ATLAS pixel detector was used to perform a commissioning test of the detector. For the first time production part of the pixel detector consisting of 144 modules, out of a total number of 1744, was completely equipped with services and managed by a initial production of the ATLAS DAQ system components.

The Endcap has been operated in an environmental chamber withing the clean room used for the ATLAS Inner Detector assembly in the CERN SR1 building.

These operation has been an important step in the commissioning of the detector, showing that the full services, the communication chain between the on-detector and the off-detector electronics, the DAQ and DCS hardware and software systems are properly integrated and capable to drive the detector.

The description of the components of the pixel detector and the readout electronics and Detector Control System will be described in detail in a Pixel Detector paper under preparation [1].

A lot of experience has been gained in SR1 running and is applied to the assembly of the final services.The results from the analysis of the performance of services are the subject of an accompanying ATLAS note **??**. That note will also contain the tests performed in order to calibrate the whole detector and prepare it for the data taking.

This note describes the results of the running of the system and the analysis of the data collected by the detector in two running modes:

1. with random triggers, in order to measure noise occupancy;
2. using a scintillator system to trigger on cosmic rays.

Noise measurements with random trigger have been taken in different conditions and are used to derive a number of useful information for understanding detector properties and tuning the simulation:

1. the amount of *fixed pattern noise*, i.e. channels with higher than normal occupancy, and the correlation between these channels and the one detected as *special* during the module acceptance tests;
2. the rate of random noise. Previous test beam operation could only put an upper limit on the level or random noise [3].
3. Time over Threshold (TOT) spectrum for noise: differently from naïve expectation, this has proven not to have a Gaussian distribution and a more complex model needs to be setup for that;
4. dependence of noise rate from operational conditions: trigger rate, depletion voltage, threshold settings.

Running with cosmics rays is used to derive information that needs a physics signal. Unfortunately the time devoted to cosmic runs was not enough to collect the statistics needed to check functionality of every single channel, but the amount of data written on disk is useful for:

1. checking the overall resolution and tracking reconstruction;
2. validating the simulation by comparing cluster size, ToT spectrum and timing distribution with what can be observed on the data and the calibration information;
3. exercising the alignment algorithms using tracks passing through overlapping regions between modules.

This effort is also the base for the next commissioning run with cosmics in the pit.

The note is organized as follows: at first a description of the setup geometry and cosmics trigger is given, then will be reviewed the results obtained with noise runs. After that the modification to the ATLAS tracking to reconstruct cosmics tracks will be described. In this section also overall tracking efficiency and rate will be computed, in addition to Monte Carlo validation using cosmics clusters and, finally, results on alignment and resolution.

# 2 Pixel EndCap A Cosmic Muon Setup

The pixel endcap A cosmic muon test [4] is using the same setup as the pixel system test in the SR1 building at CERN [5]. The cosmic test is a logical continuation of the system test with the goal of exercising the readout system, data taking and testing the offline reconstruction chain.

The aim is to collect a larger cosmic muon sample sample to reconstruct tracks passing through the detector, study their properties and perform a simple alignment of the detector using overlap regions on the pixel disks.

## 2.1 Pixel EndCap A Geometry

The pixel endcap A is one of the two end sections of the pixel inner detector, its geometry is described in [7]. It consists of three disks placed at 49.5 cm, 58.0 cm and 65.0 cm in the $z-$direction. There are 48 modules on each disk, i.e. 144 modules in the entire pixel endcap A. Each disk has 24 modules on the even (odd) side respectively. The even side is closer to the interaction point. The modules centers (i.e. the middle of the silicon wafer) are displaced by 4.276 mm according to the survey (the thickness of the disk implemented in the reconstruction software is only 4.2 mm however, the discrepancy will be discussed further in this note). The first module is positioned at 3.75° in $\varphi$, every other modules is rotated by 7.5° in r$\varphi$ plane with respect to the previous module. The centers of modules are placed at 119.17 mm in radius.

The module consists of 16 front-end chips bump bonded to the silicon wafer (average thickness of 256$\mu$m, the area (x,y) = 1.88 cm $\times$ 6.3 cm, that includes all guard rings), there are two rows of eight FE chips on each module. The active area of the sensor is (x,y) = 1.64 cm $\times$ 6.08 cm, each front end chip covers 0.76 cm $\times$ 0.82 cm, it has 16 columns of 400 $\mu$m and 2 columns of 600 $\mu$m (so-called *long*) pixels, and 160 normal plus 4 *ganged* rows of 50 $\mu$m pixels. The geometry of the module and its dimensions are well described in [8]. This is why the short side (local X direction) of the module has a 50$\mu$m pitch and the long side (local Y direction) has a 400 $\mu$m pitch with the only exception of ganged pixels. They are cross connected and receive a special treatment in the simulation/reconstruction code. The position of a module on a disk is defined by the module $\eta$ index (it is the same for the even and odd side modules of a particular layer, it is 0, 1 and 2 for disk 1A, disk 2A and disk 3A respectively) and the module $\varphi$ (it goes from 0 to 47, and we use it to distinguish front (=even), back(=odd) modules on one disk). The module $\varphi$ id can be used to calculate the $\varphi$ of the module center by using Eq. 1.

$$\varphi_c = (\varphi_{mod} + 0.5) \times 7.5 \times \pi/180 \tag{1}$$

The properties, position and status (ON=in readout, OFF=out of readout) of pixel endcap A modules is given in Figs. 1, 2, 3, 4, 5 and 6.

The (x,y) position of a pixel on pixel endcap module is defined by the $\eta$ index (local Y-axis, $\eta$ direction, column number) and $\varphi$ index (local X-axis, $\varphi$ direction, row number). There are 144 columns (coarse pitch) and 328 rows (fine pitch) on the module. The $\eta$, $\varphi$ index numbering is described in Fig. 7. The $\eta$ index increases with an increasing radius, i.e. decreasing $\eta$, and the $\varphi$ index increases with increasing global $\varphi$, i.e. it is counted in the opposite direction for the even and odd side modules. The

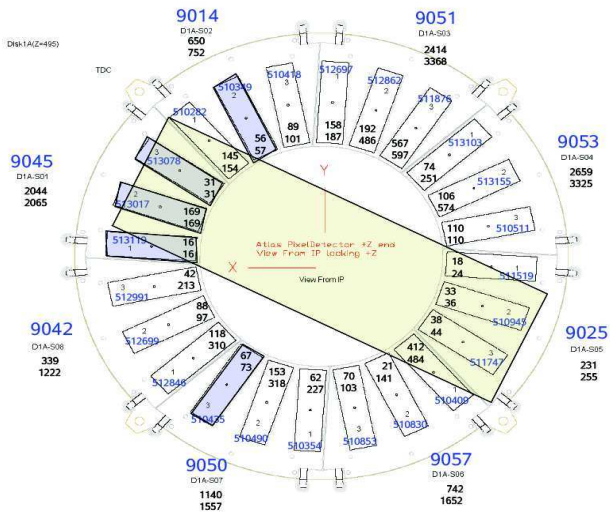


Figure 1: Disk 1A even side modules.

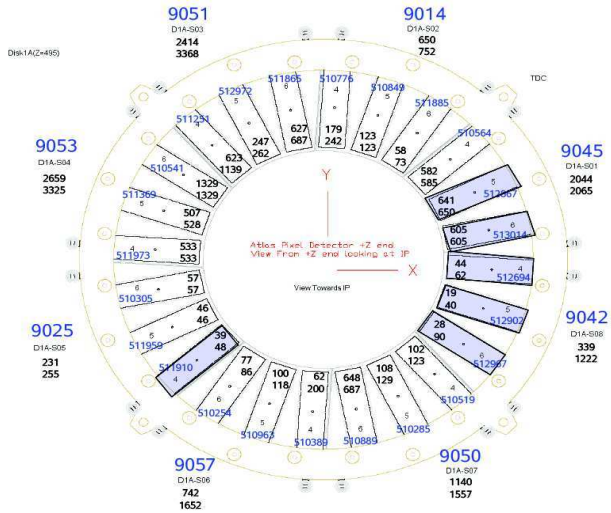


Figure 2: Disk 1A odd side modules.

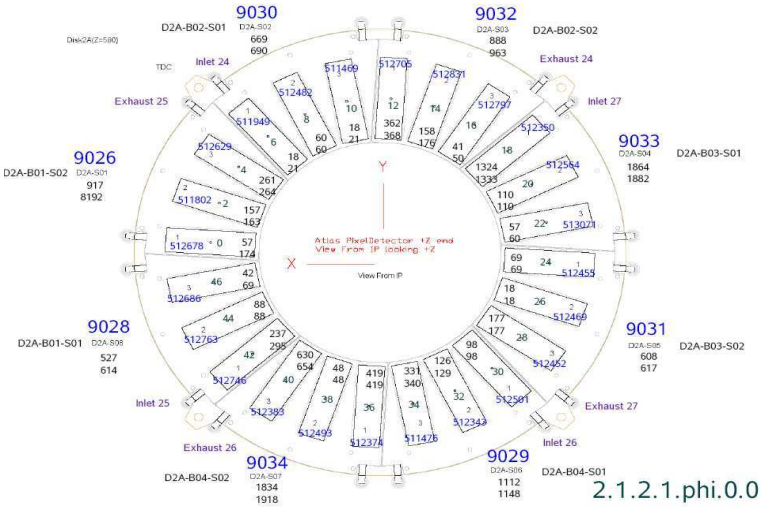


Figure 3: Disk 2A even side modules.

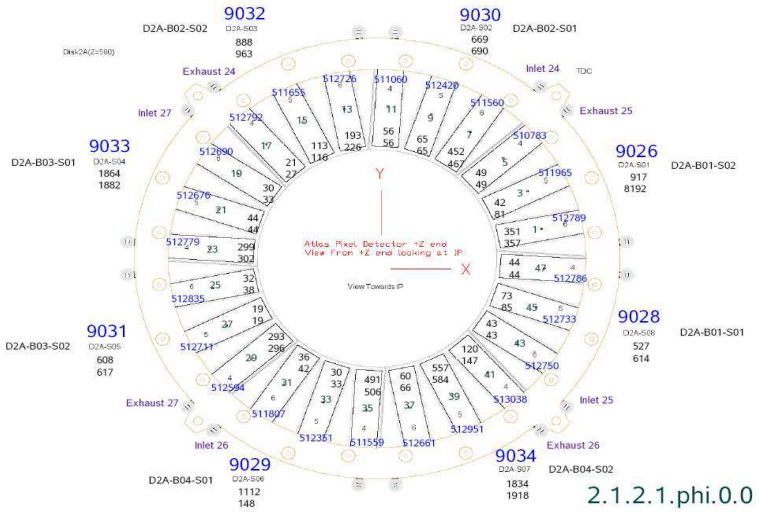


Figure 4: Disk 2A odd side modules.

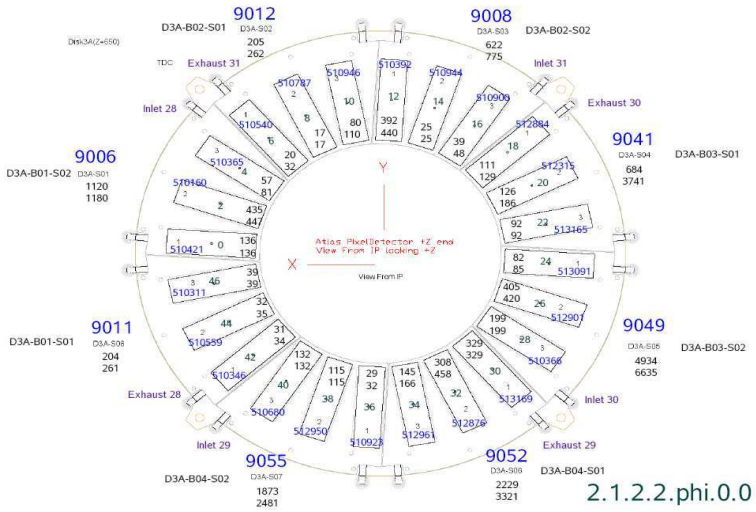


Figure 5: Disk 3A even side modules.

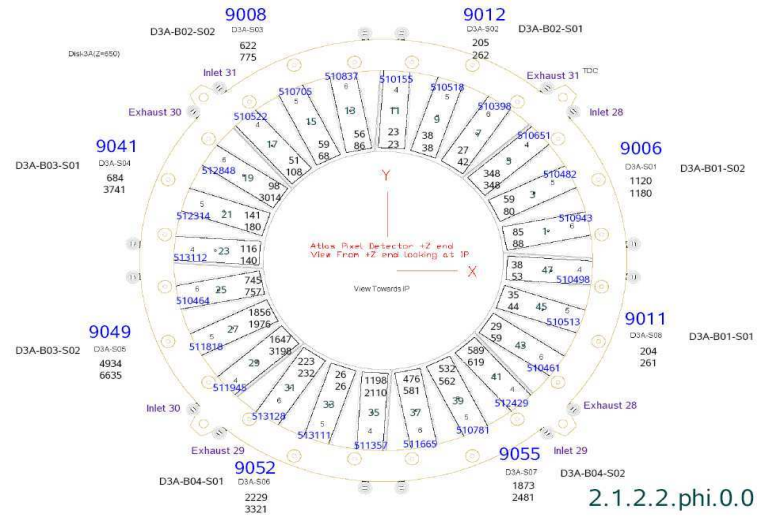


Figure 6: Disk 3A odd side modules.

same rule is also applied for the local coordinate system on the pixel endcap module with the coordinate center defined as a center of the module (that is the actual center of the silicon sensor). Note that the even module local X coordinate orientation is the same as the local X of an odd module.

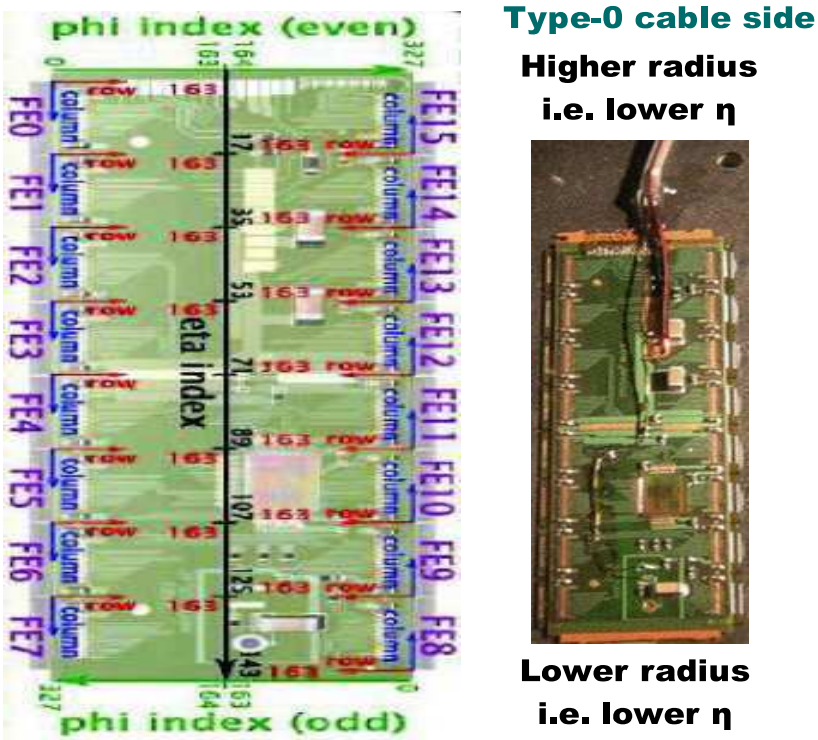


Figure 7: Definition of row and column indices on the pixel endcap module.

The global coordinate system is defined in Figs. 1, 2, 3, 4, 5 and 6.

## 2.2 Cosmic Setup

The pixel endcap A cosmic setup consists of the pixel endcap A that is hooked up inside the dry box providing the required environment for the pixel endcap operation (dry air mainly), a prototype service quarter panel (PSQP) connected to all outside services (cooling, low voltage and high voltage distribution and regulation, readout, environmental information etc.). Both the pixel endcap and PSQP are placed inside the dry box. The endcap hangs vertically inside the dry box (i.e. its axis is perpendicular to the table top), that is an obvious requirement to maximize the flux of cosmic muons passing through the pixel endcap fiducial volume as well as to maximize the number of at least 3-hit tracks.

### 2.2.1 Mechanical design

The trigger system [9] (dimensions of the system are given in Fig. 8) consists of four SLAC scintillators, two smaller scintillators are placed above each other (the top scintillator only 21 cm above the end section, i.e 23.5 cm above disk 3A or 39 cm above disk 1A and the bottom scintillator 120.0 cm below the top one, i.e. 96 cm below the disk 3A). The small scintillators (45.8 cm $\times$ 71.2 cm) are centered

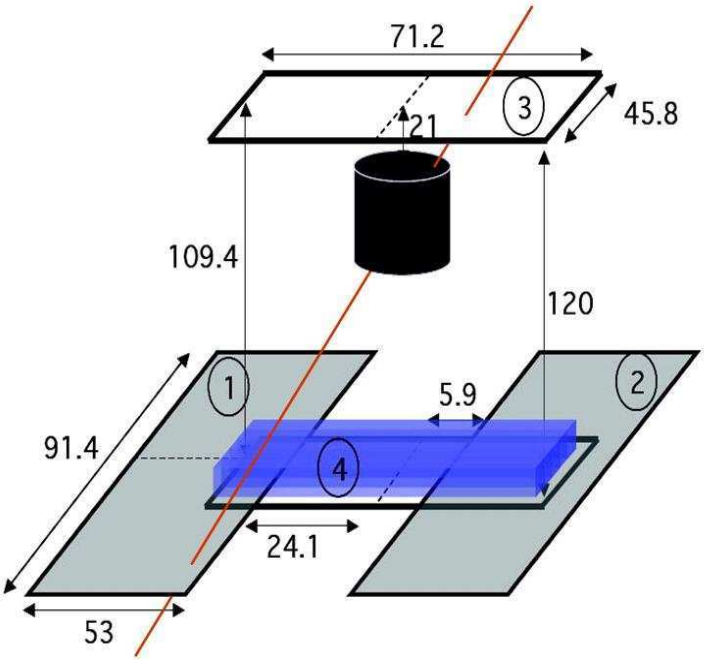


Figure 8: Schematics of a pixel endcap A cosmics setup.

around the z-axis of the end section. The top scintillator is referred to as scintillator no. 3 and the bottom one as scintillator no. 4. These two scintillators are the bare minimum to have a good coincidence circuit (described in Fig. 12), the top scintillator is required to trigger the cosmic muon and the bottom scintillator defines geometrically the acceptance of the trigger system. There are many muons that leave the signal in scintillators 3 and 4 but never pass through the pixel endcap or leave only one/two hits. The endcap A is rotated by $-\pi/8$ with respect to the y-axis of the dry box (the y-axis of the dry box is parallel to the long side of the dry box table, i.e. axis of the PSQP). This rotation can be seen in Fig. 1.

Additionally, we had a luxury of additional two large scintillators that improve the trigger efficiency of the system. The ideal placement of large scintillators (referred to as scintillator 1 and 2) would be on the sides of the dry box so that they can cover even large incidence angles, see Fig. 9 for such an ideal topology. This placement however turned out to be very difficult to implement because of the access to the pixel endcap during the system test operation. At the end, we have decided to place large scintillators under the table top of the dry box. The dimensions of large scintillators are 53.0 cm $\times$ 91.4 cm.

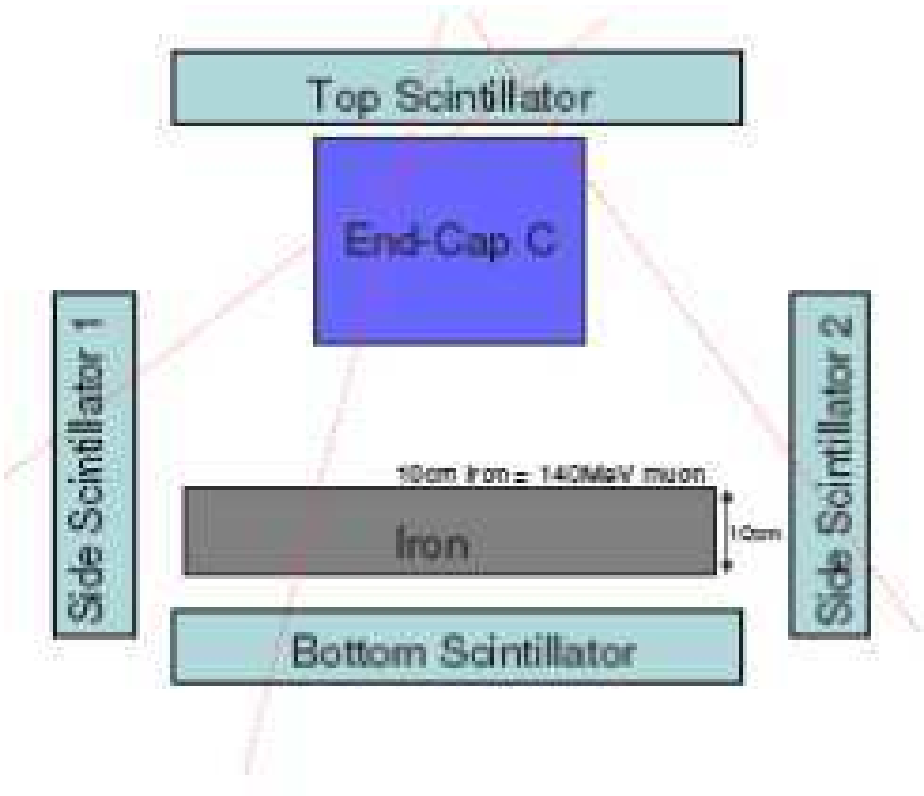


Figure 9: Schematics of an ideal pixel endcap A cosmics trigger system setup.

Whereas the placement of top and bottom small scintillator is naturally determined by the length (or height in this particular case) of the endcap, the height of the PSQP and by the access essentially required to connect exhaust copper extension tubes to the endcap cooling pipes, in order to decide what is the optimal placement of large scintillators, we had to run a toy Monte Carlo simulation to make a decision. The results of this simulation are presented in Fig. 10.

The aim of this study was to maximize the weighted hit density coverage on the surface of the bottom

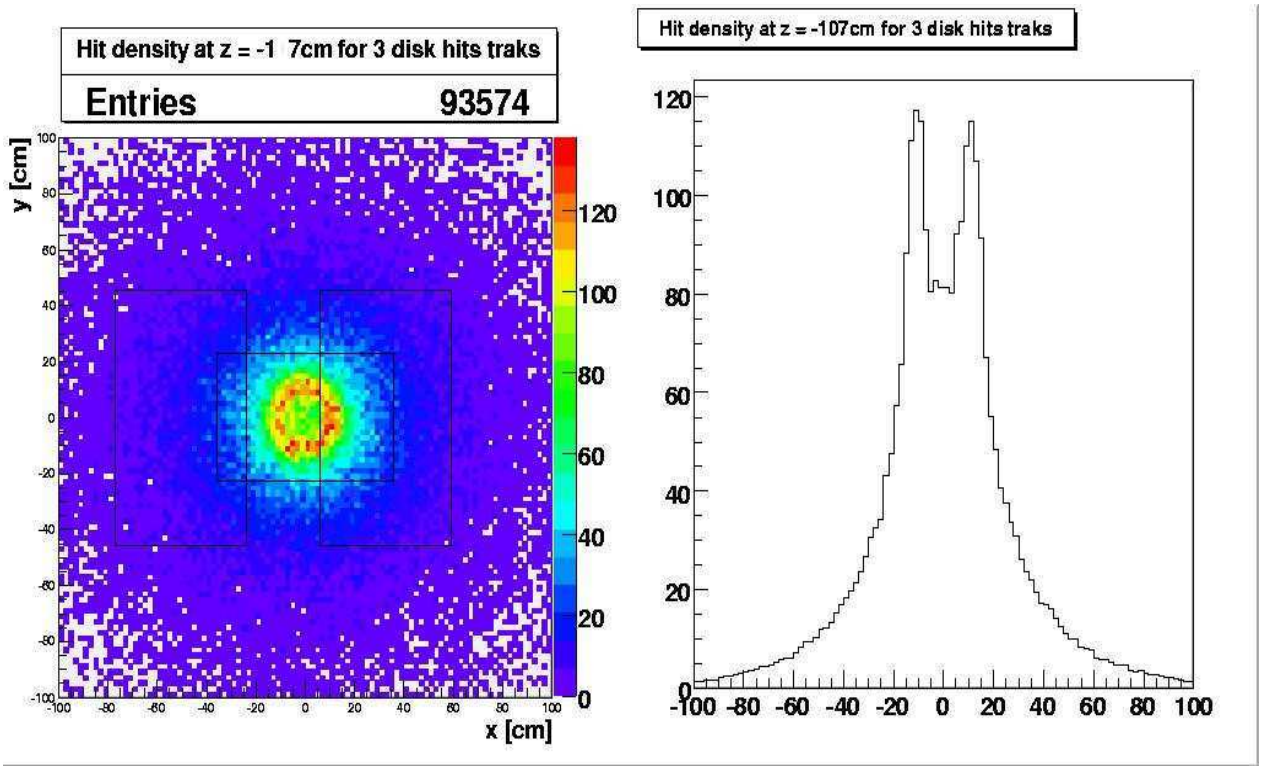


Figure 10: Toy Monte Carlo study dedicated to optimize the large scintillator placement.

large scintillators (left plot in Fig. 10). At the same time, there are further restrictions for the placement of bottom large scintillators, such as: (a) they cannot be possibly centered around the axis of the pixel endcap because of legs of tables holding the endcap dry box, (b) the bottom small scintillator itself that is only 11.5 cm above the large scintillators, (c) the mounting brackets of the frame of large scintillators. The ideal placement (see Fig. 11) is perpendicular to the small scintillators only 11.5 cm above the bottom scintillator. Due to the reason outlined above, there is a placement offset along the y-direction (i.e. long side of the table, small scintillators), which is 24.1 cm with respect to the pixel endcap z-axis (and the center of small scintillators) for scintillator no. 1 and 5.9 cm in the opposite direction for scintillator no. 2.

To remove low momentum cosmic muons which suffer most from the multiple scattering, we have also investigated the possibility to filter them out by an extra layer of iron between scintillators 3 and 4, directly below the endcap. Due to the support of PSQP, we had a possibility to break the iron layer into two parts: one above the endcap and the other below the PP0 panel of the PSQP. The maximal thickness that we could place on the table would be less than 300 kg. We could not put there more because more than $\sim$750 kg would compromise the safety of the device due to the extra weight concentrated on the building floor and the table itself. Another constraint was very little space under the PSQP. There was something like 15 cm of space between the rails that hold the PSQP, we could not use more than $\sim$12 cm because the iron had to be inserted manually and we had to be very cautious about damaging the PSQP. Finally, only $\sim$12 cm of iron in the forward region of the setup was compromised. That is an equivalent to saying that we are cutting out all muons under 140 MeV. In order to reduce the multiple scattering significantly we would need at least $\sim$500 MeV cutoff.

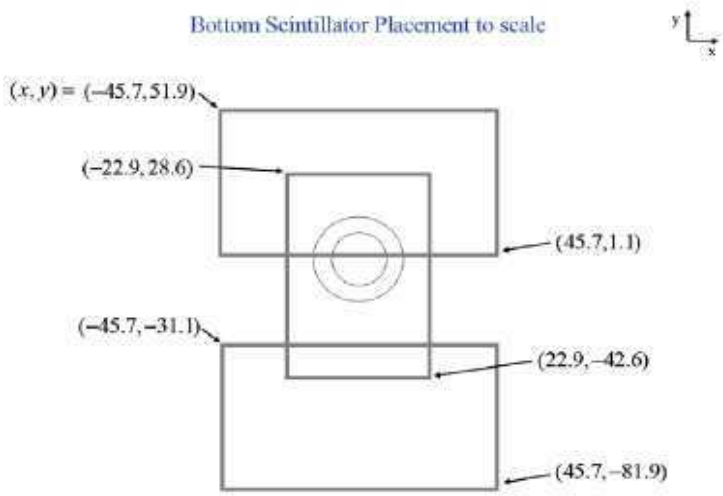


Figure 11: Placement of large scintillators, view from the top, towards interaction point.

### 2.2.2 Coincidence circuit

The layout of a coincidence circuit is given in Fig. 12. The starting point is to require a signal in the top scintillator (scintillator no. 3) and require logical *AND* with logically *OR* of all bottom scintillators (one of them is the small bottom scintillator, and two are the large ones in the front and back of the setup).

In the cosmic trigger and readout system we had three crates (the following describes an ideal signal path):

- *NIM crate*: it was a crate with all the HV power supplies for the PMT tubes in the setup and the logic electronics (discriminators, delay units and AND/OR units). The main idea was to keep the discriminators close to the setup so that we avoid any attenuation over the long distances and only transfer the TTL signal from the discriminators over more than 50 m long cables. This crate was about 2 meters away from the setup, inside the clean room of the SR1 building. The final output of the AND logical unit comes out of the crate as an input for TDC in the VME crate in the rack area, it is actually equivalent to L1A Trigger accept in the real experiment.

- *VME crate*: this is a crate that holds SBCs, LTP, TTC and a BUSY unit (OR). The TDC receive TTL signal from discriminators and AND/OR logic unit, and in principal we could use this information for some timing study. However, we never got a chance to do it and this information is not available offline. This is why only the output of the AND/OR unit is received by LTP, transfered to TTC and finally to TIM in the ROD/DAQ crate.

- *DAQ crate*: it consists of several RODs (12 RODs needed to readout all 144 modules in endcap A) and TIM. The trigger signal from TTC (in VME crate) goes to TIM and then gets distributed among RODs. In the reality we had 2 DAQ crates, one with 8 RODs and the other with 4 RODs.

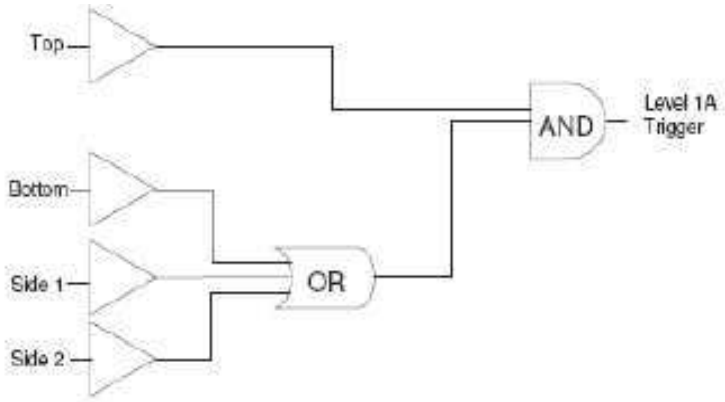


Figure 12: Coincidence circuit.

### 2.2.3 Cosmic muon rate

The expected cosmic muon rate was studied extensively using the toy Monte Carlo simulation, full ATLAS Pixel Detector simulation and cross-checked with the back of the envelope calculations.

The integral intensity of vertical muons above 1 GeV/c at sea level is 70 $m^{-2}s^{-1}sr^{-1}$ [10]. It is an equivalent of 1 cosmic muon per $cm^2$ every second. The distribution of cosmic muons is roughly $\cos^2\theta$ of the incidence angle, it is symmetric in $\varphi$, the mean of the cosmic muon momentum on the sea level is $\sim 4$ GeV/c.

The toy Monte Carlo start with a randomly distributed cosmic muon passing through the top level scintillator, it assumes the $\cos^2\theta$ incidence angle distribution, and a full symmetry in the $\varphi$ angle. It has a flat momentum distribution. No detector effects are assumed, this is why this assumption is sufficient to estimate the cosmic muon rate. The overall trigger efficiency is expected to be close to 85 % and the disk hit efficiency is roughly 90 %. We count how many times the cosmic muon will pass through the bottom scintillator(s) and how many hits will be associated to a muon traversing the fiducial volume of the endcap given the geometry of the detector.

The full ATLAS pixel detector simulation takes all the detector effects into account. We start with the cosmic muon generated in cosmic muon generator (it has all angular and momentum distributions simulated correctly), count how many times do we have a coincidence in the top and bottom scintillators, simulate the response of the detector to cosmic muon passing through the sensitive layers, build space points/hits and reconstruct tracks. We also count the number of tracks and hits on the tracks to estimate the trigger rate and the track reconstruction efficiency (convoluted with the detector acceptance indeed).

The toy Monte Carlo estimates the cosmic muon rate through the top scintillator is 54 Hz and the trigger rate with all four scintillators is 16 Hz.The full detector simulation gives 6 Hz for the coincidence of top and bottom scintillator and 18 Hz for all four scintillators. These two values are in a good agree-

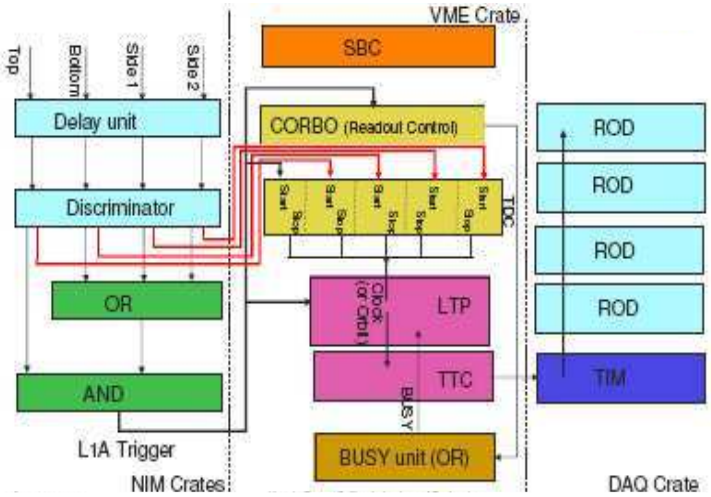


Figure 13: Ideal signal path.

ment with the trigger rate measured in the DAQ system, we have recorded cosmic data with a data taking frequency of about 15 Hz.

The track reconstruction efficiency (again, convoluted with the detector and setup acceptance), if all 144 modules are readout, estimated from the simulated data was expected to be in the vicinity of 6 %, i.e. we would expected roughly one three hit cosmic muon track every second. In the reality, only 115 modules were readout, some disabled modules have clustered in space (e.g. the whole sector, i.e 6 modules, were disabled) and that is why the track reconstruction should be 20-30% lower than that, i.e. $\sim$4%. This is really what we have measured in the data, $\varepsilon = 3.8\%$ (see following sections of this note). The ideal cosmic muon rate for at least 3-hit tracks is 1.5 Hz, and probably about 1 Hz for the detector with 29 disabled modules.

The track properties are affected by our choice of the cosmic trigger system layout. For example, the fact that the small scintillators are rectangular will deform the initial flat angular $\varphi$ distribution into a sin wave distribution. The fact that the scintillators are rotated with respect to the end section by $\pi/8$ will shift the $\varphi$ angular distribution by this amount to the negative side. Another interesting feature is that modules missing in the readout will create dips in the angular $\varphi$ distribution (see the following section of this note for details). There were many reasons for having that many modules disabled from the readout: disconnected cooling loop, malfunctioning opto board, missing bias voltage, missing NTC reading, etc. All these effects were also implemented in the detector simulation, see Fig. 14.

## 2.3 Cosmic setup simulation

The goal of the simulation chain is to preserve existing ATHENA structure and geometry of packages as much as possible without introducing too many changes. The reason is that one of the cosmic test priorities is to validate the simulation/reconstruction chain from the beginning to the end, i.e. from simulation, digitization, bytestream converter all the way to reconstructed tracks and alignment. This is why if we find any abnormalities, bugs or mistakes, we would like to correct them, and make them part of ATHENA release 13. We have quite successfully managed all that with the only exception of using the combined test beam standalone tracking code with no magnetic field, that is not part of the official

release 13.
The full ATLAS cosmic setup simulation is done in the following five steps:

- *cosmic muon generator*: cosmic muons get randomly generated according to all distributions described in [10] in *CosmicGenerator* package [11]. The core of the package is an old Fortran cosmic muon generator inherited from previous experiments that is wrapped up inside the C++ code to provide the necessary interface with other ATHENA simulation packages.

- *pixel endcap A geometry*: the pixel endcap A geometry is identical to the one implemented in *PixelGeoModel* [12]. The only difference is that one has to switch off endcap C, the barrel of the pixel detector, pixel support tube, frame and services. The whole pixel detector is essentially reduced to endcap A only.

- *GEANT 4 detector simulation*: the GEANT 4 (G4) is described mainly in *G4AtlasApps* package [13]. It contains definition of all setup positions and dimensions (pixel endcap position, scintillator and iron positions/dimensions etc.). The pixel endcap A (or the pixel detector that is reduced to pixel endcap A) is positioned in its nominal position.

- *trigger system simulation*: the scintillators are placed in the right position in *G4AtlasApps*, when the cosmic muon passes through their fiducial volume, the energy is deposited in that volume and if it is above some minimum amount it is considered to be a hit in the scintillator system. The logic coincidence between two scintillators is implemented in *InDetCosmicSimAlgs* package [14]. Events where there is no coincidence between top and logical OR of bottom scintillators are skipped, only triggerable events are passed further to digitization.

- *digitization*: the digitization code is the same as it is currently implemented in release 13, the only difference is that one has to make sure that hits from modules that are not present in readout (that includes pixel endcap C and barrel modules) are not being digitized. That would cause runtime errors.

The whole simulated pixel endcap A cosmic setup can be seen in Fig. 14 bottom, and 15. The how to run the simulation code instructions are described in [16].

# 3 Study of Noise Data

For the study of the noise in endcap A several runs were performed with various trigger signals that initiated by either a cosmic trigger or an external clock(random trigger). The data from several of these runs was analysed for characteristics of the noise signal. Maps of the hits on each module were used to study the correlation between the positions of noise hits in the data and the positions of pixels that had been marked as special during the production tests of the individual modules. Figure 16 shows a comparison of the noise levels for the modules of endcap A determined from threshold scans during the production and system tests. One can see that while the noise level in the system test is slightly higher than in the production test the results generally agree well with each other.

## 3.1 Results from Run 1125 with Cosmic Trigger

The noise occupancy in Run 1125 was computed for pixels associated to different L1-triggers, or bunch crossing id's (*BCID*), where $BICD = 5$ corresponds to the cosmic muon signal. The *module* occupancy is defined as the percentage of pixels per module per event read out, and it was computed for each of the

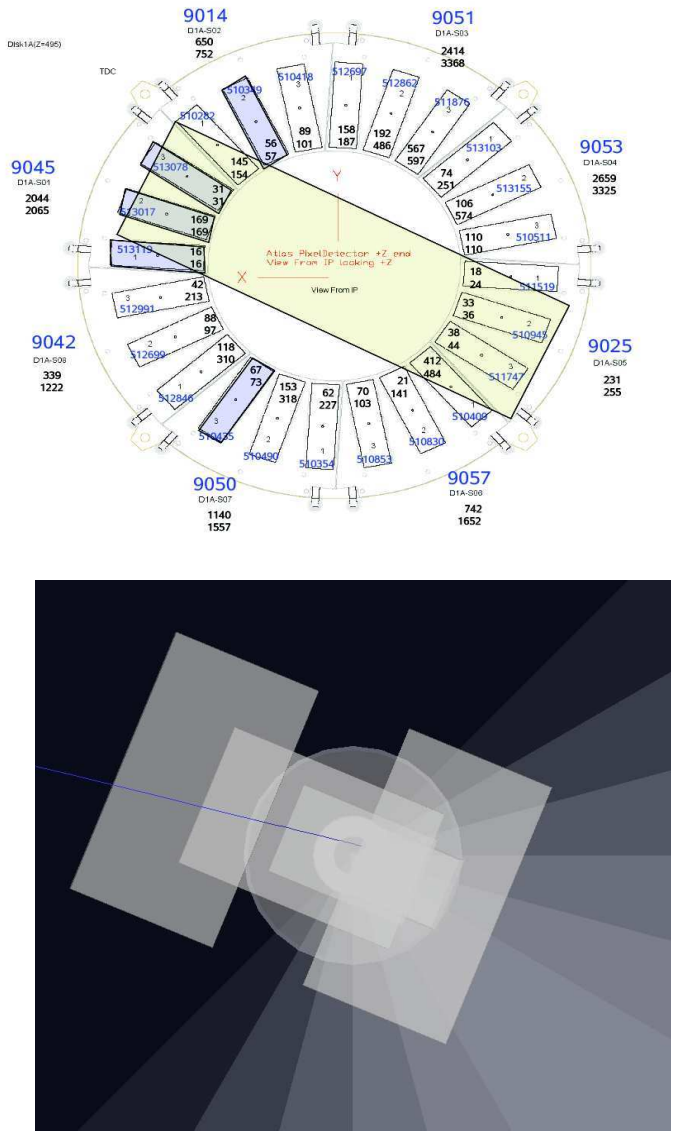


Figure 14: Simulation of the pixel endcap A cosmic setup, comparison to disk 1A, front side with small scintillator orientation. The scintillator is not up to scale.

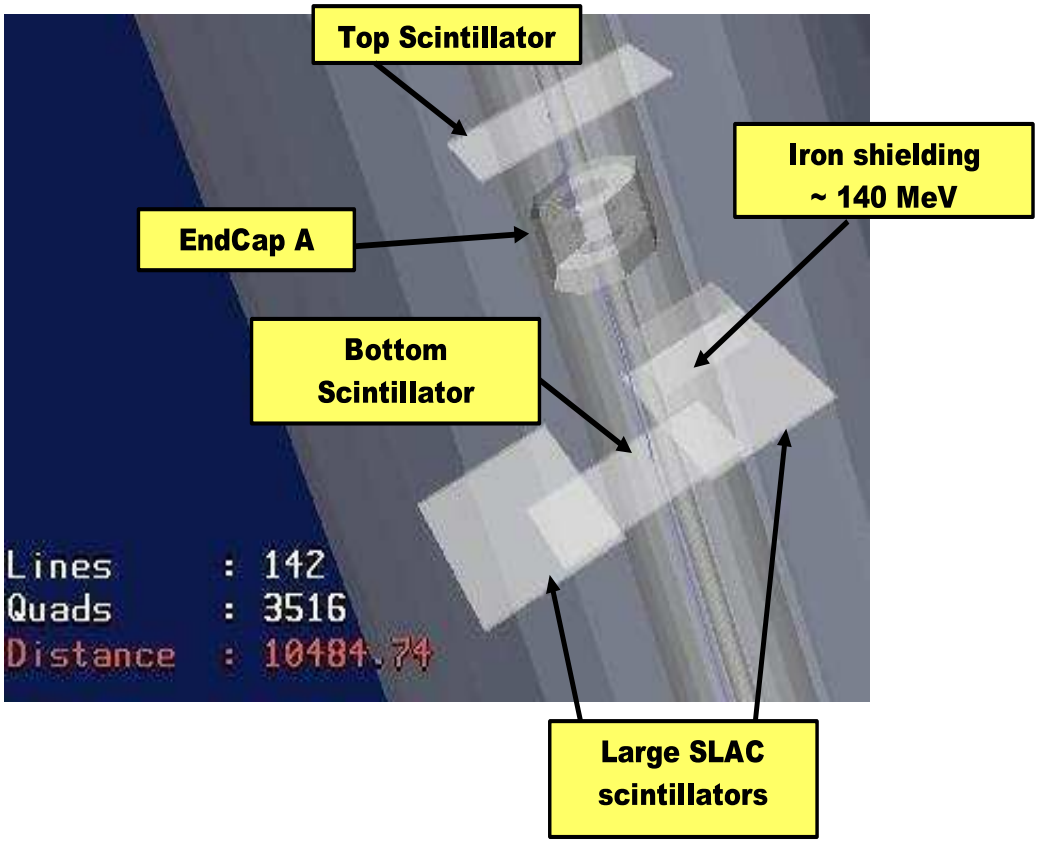


Figure 15: Simulated pixel endcap A cosmic test setup with a cosmic muon passing through it.

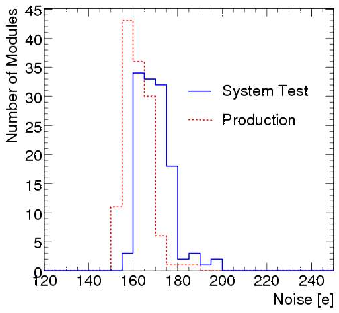


Figure 16: Noise in electrons for the modules of endcap A as determined from threshold scans during the production and system tests

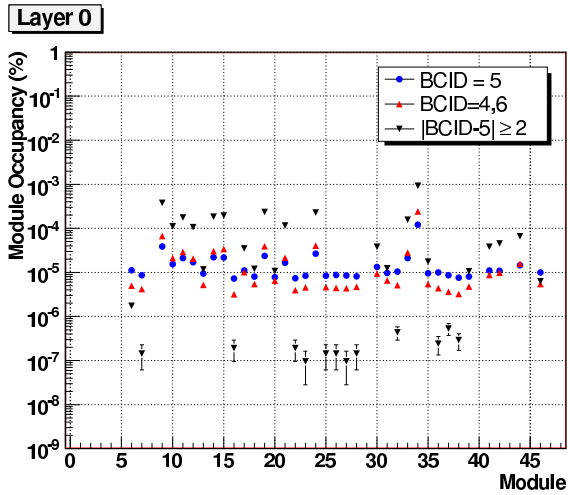


Figure 17: Module occupancies in layer 0 of endcap A during run 1125, for different L1-triggers.

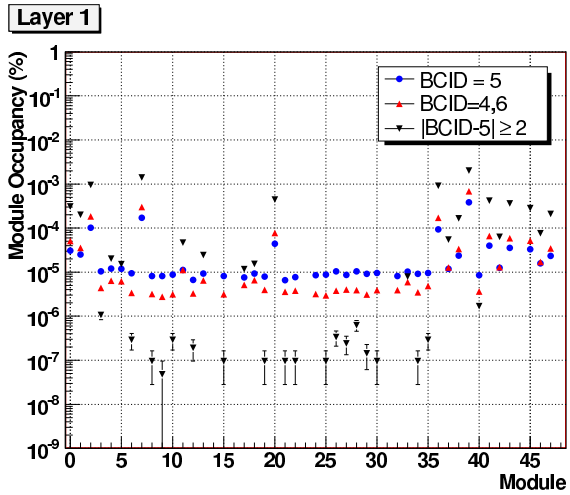


Figure 18: Module occupancies in layer 1 of endcap A during run 1125, for different L1-triggers.

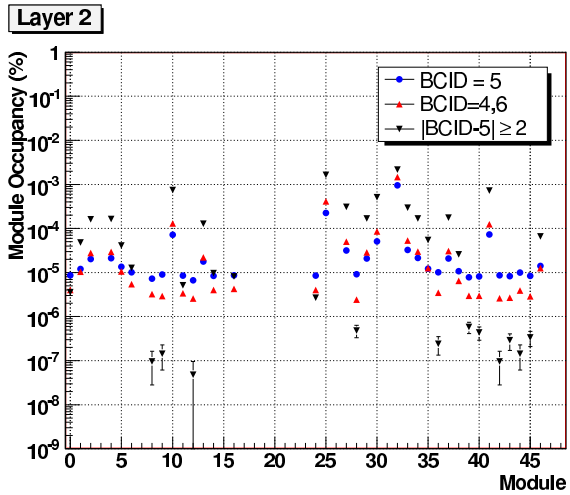


Figure 19: Module occupancies in layer 2 of endcap A during run 1125, for different L1-triggers.

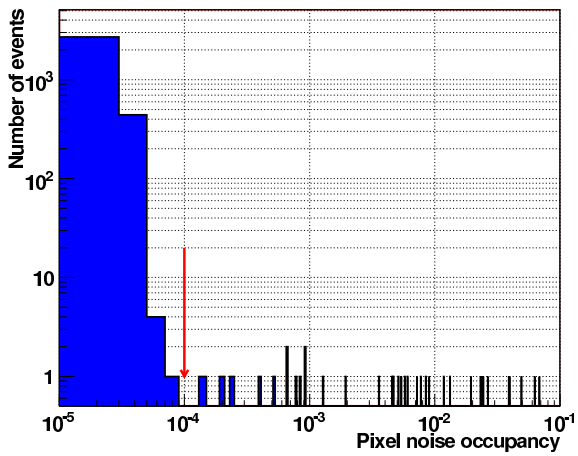


Figure 20: Pixel occupancy for low occupancy modules in endcap A layer 0.

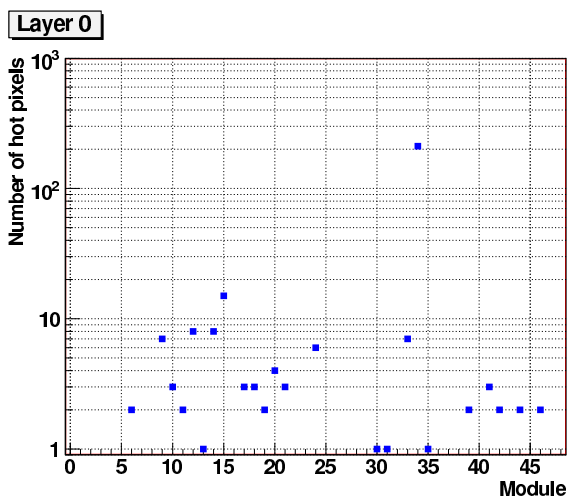


Figure 21: Distribution of hot pixels in endcap A layer 0.

three endcap A layers, as shown in Figures 17, 18, and 19. There are large fluctuations in occupancy, in particular for events not trigger by the cosmic muons, due to the presence of hot (noisy) pixels.

The pixel occupancy, defined as the number of hits in a given pixel divided by the number of events, for several modules in layer 0 with low occupancy is shown in Figure 20.

Based on Figure 20, pixels having an occupancy greater than $10^{-4}$ were defined as *hot* pixels. With this criteria, 1544 pixels were masked as hot pixels. Figures 21, 22, and 23 show the distribution of hot pixels for each module of the three endcap A layers.

The *BCID* of all selected (good) and hot pixels is shown in Figures 24, and 25. As expected, hot pixels generated by noise are not correlated with any L1-trigger, whereas all signal pixels cluster around the cosmic peak corresponding to $BCID = 5$.

The topology of the hot pixels within a module was investigated by looking at the distance (in units of row and column) between a hot pixel, and the closest and second closest hot pixel, as shown in Figures 26, and 27. The significant peaks at 1 indicate the presence of small *clusters* of nearby noisy pixels.

An example of such cluster of hot pixels in module 34 of layer 2 can be seen in Figure 28.

After removing all hot pixels in this run, the pixel module occupancy becomes very uniform within modules of a same layer, as it can be seen from Figures 29, 30, and 31. The pixel noise occupancy per module is of the order of $10^{-7}\%$.

The distribution of number of pixels per event before and after hot pixel removal is shown in Figures

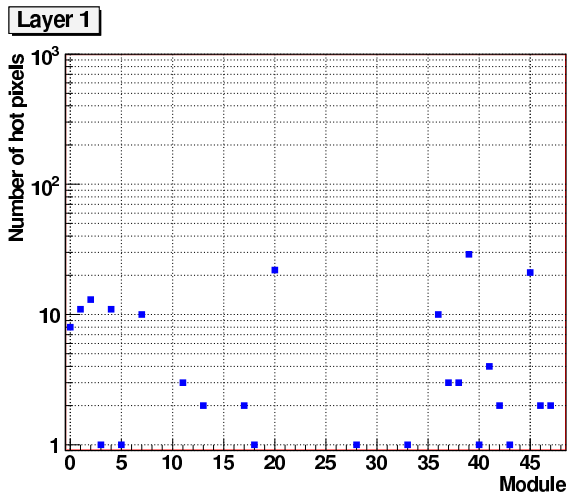


Figure 22: Distribution of hot pixels in endcap A layer 1.

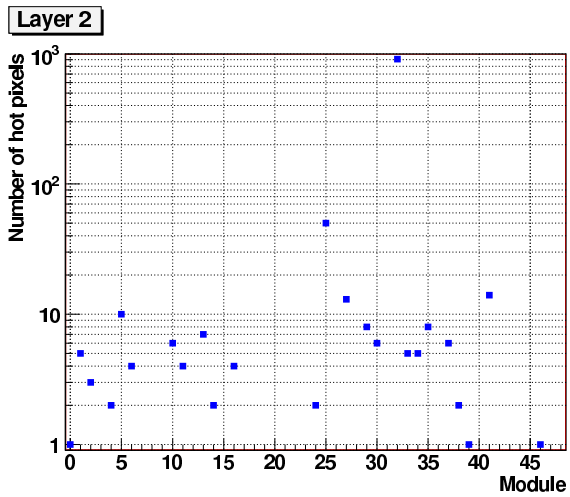


Figure 23: Distribution of hot pixels in endcap A layer 2.

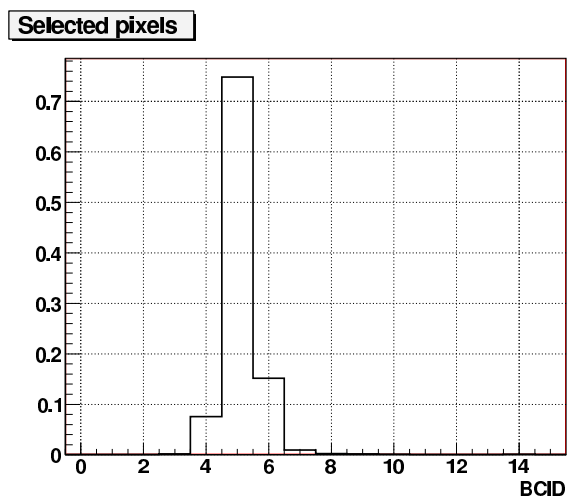


Figure 24: Bunch Crossing ID for all selected pixels not masked as hot.

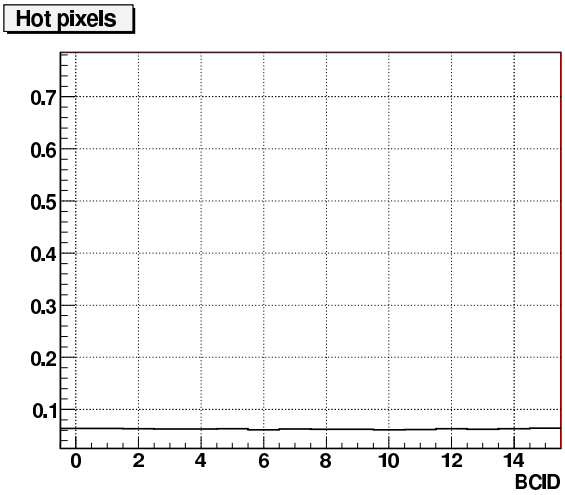


Figure 25: Bunch Crossing ID for hot pixels.

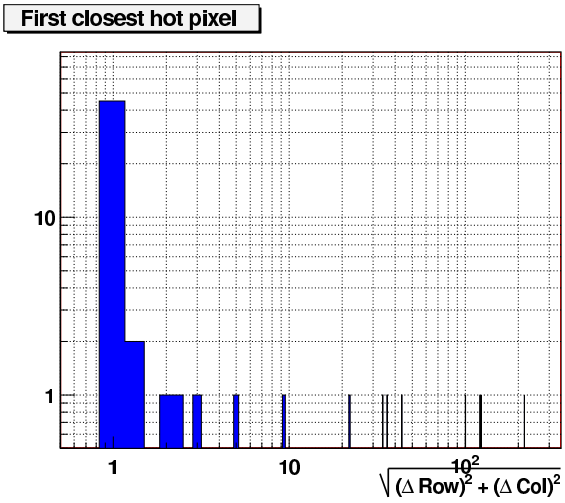


Figure 26: Distance between a hot pixel and the closest hot pixel within a module.

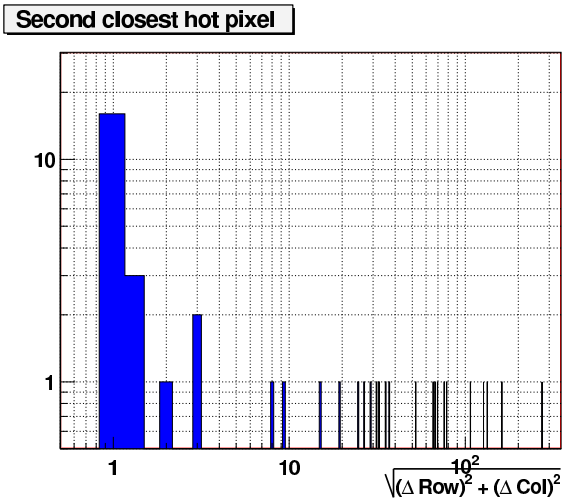


Figure 27: Distance between a hot pixel and the second closest hot pixel within a module.

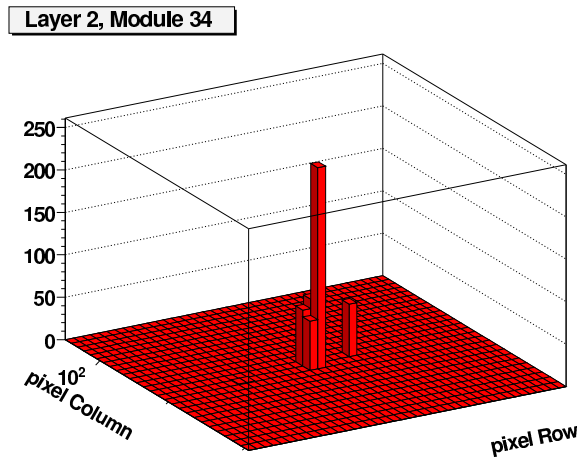


Figure 28: Example of a cluster of hot pixels in module 34 of endcap A layer 2.

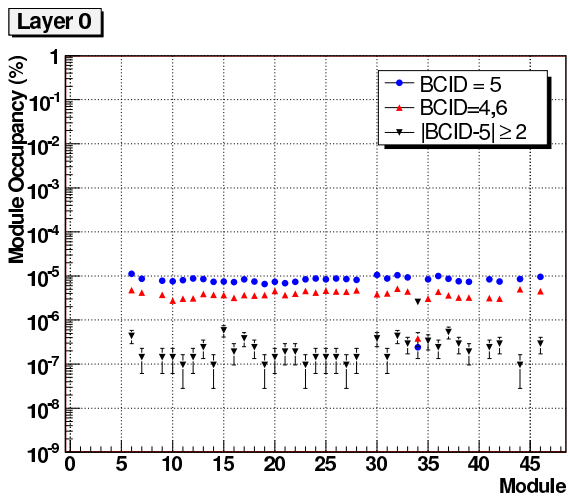


Figure 29: Module occupancies in layer 0 of endcap A during run 1125, for different L1-triggers and after hot pixel removal.

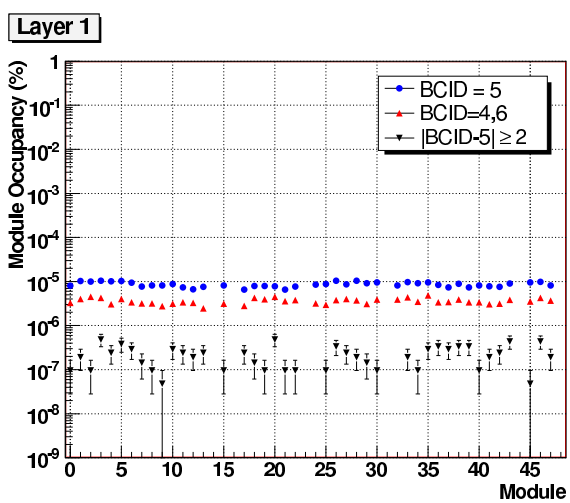


Figure 30: Module occupancies in layer 1 of endcap A during run 1125, for different L1-triggers and after hot pixel removal.

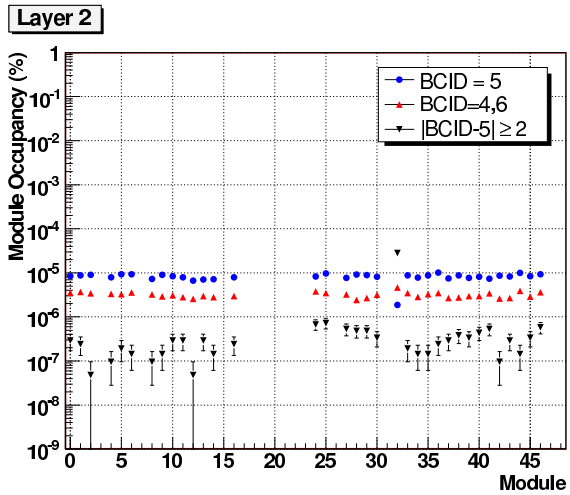


Figure 31: Module occupancies in layer 2 of endcap A during run 1125, for different L1-triggers and after hot pixel removal.

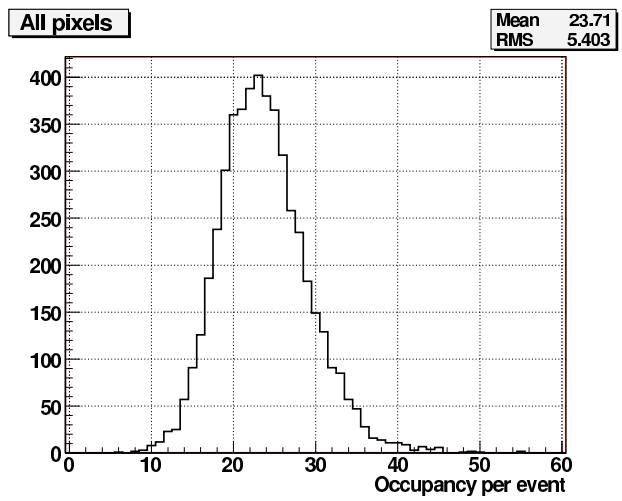


Figure 32: Distribution of total number of pixels per event.

32, 33, and 34. On average, there were 24 pixels read out per event, of which 23 were hot pixels.

## 3.2 Results from Run 1131 with Random Trigger

Run 1131 was performed with an external trigger signal at a frequency increasing from 10 Hz to 15 kHz and then decreasing back to 10 kHz. A single level 1 accept signal was used. The number of events in the run is 14 147 494.

The distribution of the occupancies for the individual pixels is shown in figure 35, with the occupancy being defined as the number of hits in a component, in this case one pixel, divided by the number of channels in the component and by the number of events in the run. Taking into account that approximately 20 modules were disabled for the run, most of them due to problems with the tuning of the optical readout chain, the occupancy for the endcap in this run is $2.5 \cdot 10^{-7}$.

Using the occupancy information it is possible to define pixels as being "noisy". In the following, all pixels with an occupancy greater than $10^{-4}$ are defined to be noisy pixels. With this definition there are 871 noisy pixels in endcap A. By excluding the noisy pixels from the analysis the occupancy for the endcap can be reduced by more than 98 % to $4.8 \cdot 10^{-9}$.

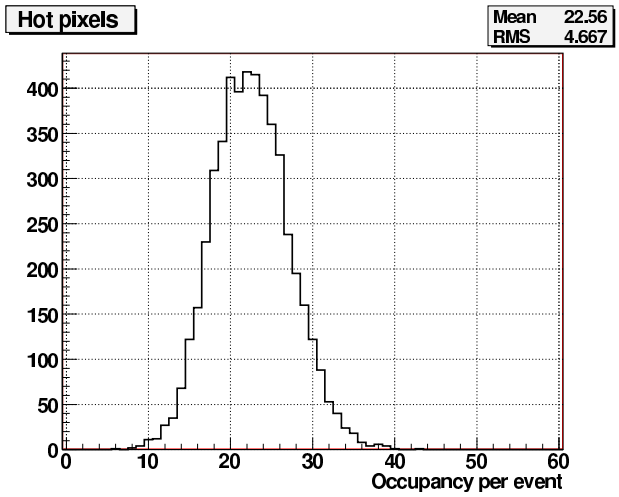


Figure 33: Distribution of number of hot pixels per event.

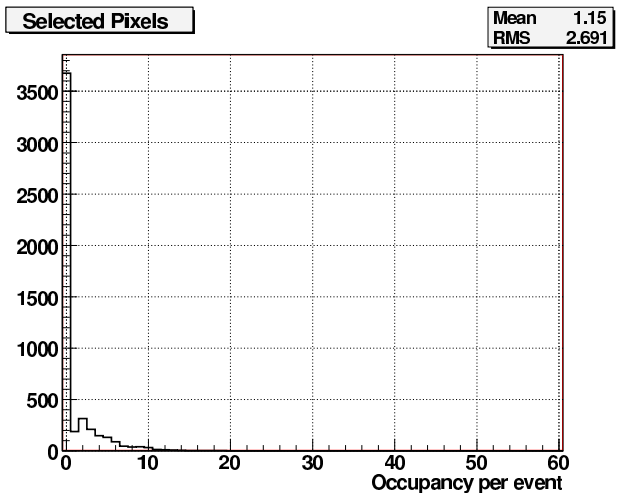


Figure 34: Distribution of number of selected pixels per event.

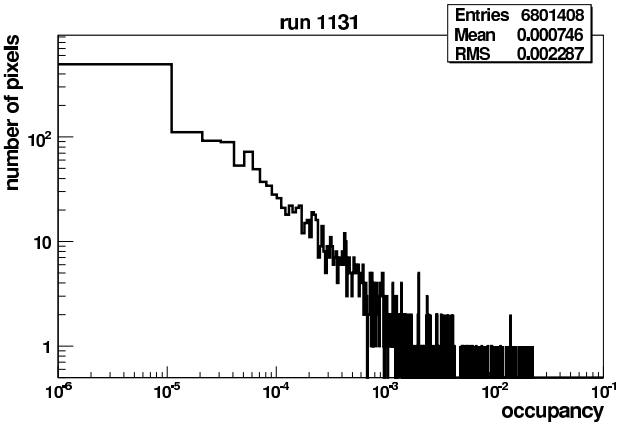


Figure 35: Distribution of the occupancies for individual pixel in endcap A during run 1131. The occupancy is defined as the number of hits in a pixel in the whole run divided by the number of events in the run.

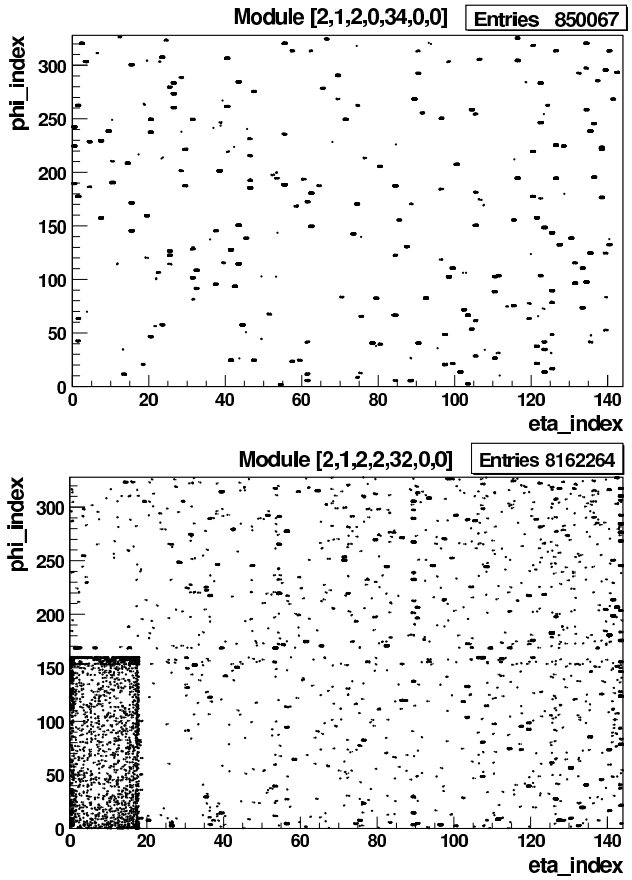


Figure 36: Hit maps for two modules with high noise levels in run 1131.

There were two modules with unusually high noise levels in this run, modules [2,1,2,0,34,0,0][1)] and [2,1,2,2,32,0,0][2)] which together contained 568 of the 871 noisy pixels. Maps of the hits for those two modules are shown in figure 36. More than 40 % of the hits in the run are found on module [2,1,2,2,32,0,0].

The positions of noisy pixels were compared to the positions of pixels that had been marked as being special during the production ("FLEX") tests of the individual modules. Table 1 gives an overview of the convention for the description of the pixel status used in the offline software and the numbers of pixels with each condition as determined in the production tests. The comparison shows that most of the noisy pixels had been marked as special in the production tests. Excluding the two modules with high noise levels, 283 of the remaining 303 noisy pixels are special, which corresponds to 93 %. 273 of those pixels have bits 0 and 13 set, meaning that the threshold is not tunable and that they do not yield useful data. Table 2 gives an overview of the numbers of status bits for the 303 noisy pixels.

A distribution of the time-over-threshold for all the hits in the endcap is shown in figure 38. One can see that the distribution has a maximum at 5 bunch crossings, or 125 ns, and a tail up to 30 bunch crossings, or 750 ns, and more.

### 3.3 Results from Run 1153 and 1144 with Special Setting

Run 1153 was performed with an effective trigger rate of about 12 kHz. A single level 1 accept signal was used. The number of events in the run is 16 776 587. In this run, two modules, [2,1,2,0,14,0,0][5)]

[1)] offline ID [2,1,2,0,34,0,0], serial number 510853, geographical IDs D1A-S06-M3, D1A_B04_S1_M3
[2)] offline ID [2,1,2,2,32,0,0], serial number 512876, geographical IDs D3A-S06-M2, D3A_B04_S1_M2
[3)] offline ID [2,1,2,1,39,0,0], serial number 512951, geographical IDs D2A-S07-M5, D2A_B04_S2_M5
[4)] offline ID [2,1,2,2,41,0,0], serial number 512429, geographical IDs D3A-S07-M4, D3A_B04_S2_M4
[5)] offline ID [2,1,2,0,14,0,0], serial number 512862, geographical IDs D1A-S03-M2, D1A_B02_S2_M2

| bit | meaning | description | numbers of pixels endcap A | detector |
|---|---|---|---|---|
| 0 | use code | 0 =useful data, 1 =not useful data: black out pixel in reconstruction | 4938 | 129231 |
| 1 | off for data | set to one if pixel is masked by DAQ | 326 | 5908 |
| 2 | off for calibration | set to one if pixel is masked during calibration runs | 0 | 0 |
| 8 | digitally dead | bit 0 of ModuleAnalysis mask: must trigger bit 0 | 71 | 57345 |
| 9 | disconnected bump | bit 1 of ModuleAnalysis mask | 1528 | 29511 |
| 10 | merged bump | bit 3 of ModuleAnalysis mask | 173 | 1437 |
| 11 | dead with particles | bit 5 of ModuleAnalysis mask: must trigger bit 0 | 4173 | 61852 |
| 12 | low efficiency with particles | bit 6 of ModuleAnalysis mask: must trigger bit 0 | 4255 | 62731 |
| 13 | threshold not tunable (analog dead) | bit 11 of ModuleAnalysis mask: must trigger bit 0 | 2675 | 42567 |
| 14 | ToT not tunable | bit 14 of ModuleAnalysis mask | 2543 | 37257 |
| 15 | noisy pixel | bit 16 of ModuleAnalysis mask: must trigger bit 0 | 17 | 634 |
| 16 | unknown dead | any pixel with bit 0 set and bits 8-15 not set | 0 | 2144 |
| 25 | bottom neighbour special | bottom=smaller row number | 3179 | 90192 |
| 26 | top neighbour special | | 3179 | 90192 |
| 27 | left neighbour special | left=smaller column number | 1624 | 69386 |
| 28 | right neighbour special | | 1624 | 69386 |
| any | special | pixels that have at least one bit set | 5627 | 141189 |

Table 1: List of the status bits used to describe the pixel status in the offline software. The pixel status is stored in an unsigned integer, bit $i$ in the list corresponding to the position $2^i$ in the integer. The corresponding bits used in ModuleAnalysis, where applicable, are given in column 3. For each bit the number of pixels that were assigned the corresponding status in the production ("FLEX") tests is given, both for endcap A and for the whole pixel detector. Bits that are not present in the list are not used at the moment.

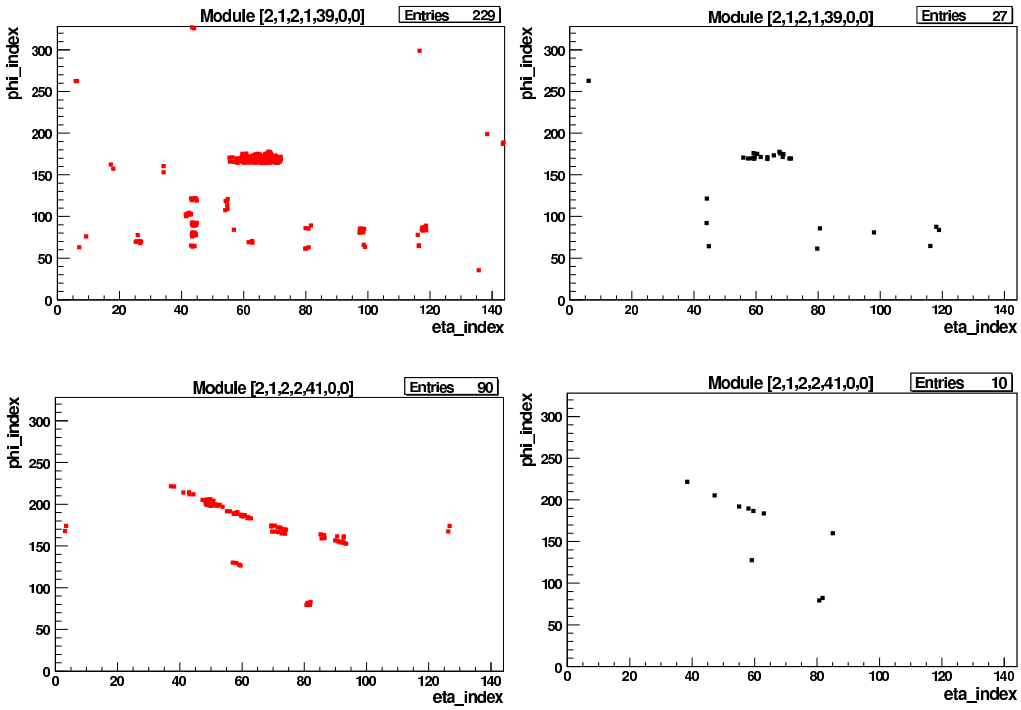


Figure 37: Scatter plots for two modules[3)4)] of pixels marked as special in the production tests (left) and of noisy pixels in run 1131 (right).

| status bit | number of noisy pixels | fraction of all noisy pixels |
|---|---|---|
| any bit, special | 283 | 93 % |
| 0, not giving useful data | 273 | 90 % |
| 1, off for data | 65 | 21 % |
| 8, digitally dead | 0 | 0 % |
| 9, disconnected bump | 0 | 0 % |
| 10, merged bump | 3 | 1 % |
| 11, dead with particles | 205 | 68 % |
| 12, low efficiency with particles | 205 | 68 % |
| 13, threshold not tunable | 273 | 90 % |
| 14, ToT not tunable | 222 | 73 % |
| 15, noisy | 0 | 0 % |

Table 2: Numbers of noisy pixels in endcap A in run 1131, excluding two modules with unusually high levels of noise, for the different status bits as determined from the production test data.

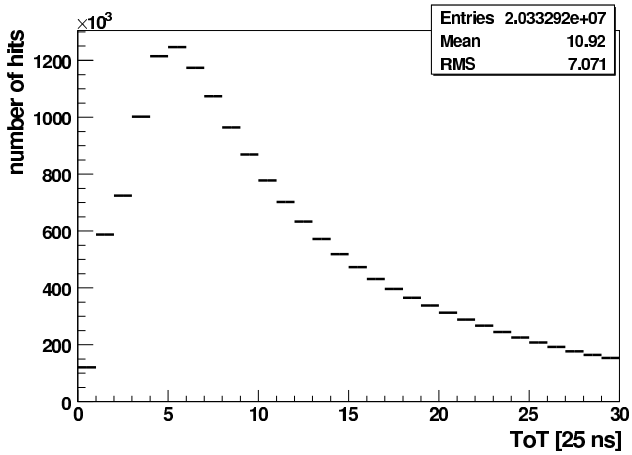


Figure 38: Distribution of the time-over-threshold for all hits in endcap A during run 1131.

and [2,1,2,2,27,0,0][6], had the threshold lowered to TDAC-25, corresponding to a change with respect to the reference value of about 1581 electrons. Module [2,1,2,0,14,0,0] shows an above average number of noise hits, but still has no hits in most of the pixels. Module [2,1,2,2,27,0,0], for which a map of the hits is shown in figure 39, shows a number of about 13 000 hits in almost every pixel. The pixels in the first four rows of every chip, corresponding to a phi_index from 0 to 3 and from 324 to 327, show lower than average numbers of hits, with about 6000 hits on average for the first two rows of each chip. This can be seen clearly in figure 40. In a subsequent analysis of run 1144, in which the threshold had been lowered to TDAC-20 for all modules, three modules[7][8][9] show a similar behaviour in that they have a high number of evenly distributed hits with about half as many hits in the first two to four rows. One module[10] has a similarly high number of hits but only four front-end chips (0, 6, 8, 15) show a lower number of hits in the first four rows. Hit maps for these four modules with anomalously high noise levels are shown in figures 41 and 42. The other modules in run 1144 exhibit noise patterns that are comparable to those typically found in the runs at default settings except for a higher number of hits in the ganged pixels. Run 1144 contains 16 774 967 events in total taken at a trigger rate increasing from 5 kHz to 13 kHz. A single level 1 accept signal was used.

Several pixels on module [2,1,2,2,27,0,0] show no noise hits in run 1153. The positions of these 82 dead pixels were compared to the positions of the 372 special pixels from the production tests. 61 (74 %) of the 82 dead pixels are special. There are 61 special pixels with the status bits (0,11,12,13,14) set (no useful data, dead with particles, low efficiency with particles, threshold not tunable, ToT not tunable), 57 (92 %) of which are dead. In addition there are 5 special pixels with the status bits (0,1,13,14) set (no useful data, off for data, threshold not tunable, ToT not tunable), 4 of which are dead. These two classes of pixels contain all the pixels with status bit 14 set. None of the 306 special pixels with other combinations of status bits are dead. As this comparison shows, for this module there is an almost one-to-one correspondence between the pixels that show no noise hits and the pixels with status bit 14 set.

Four modules in run 1153 had special TDAC pattern masks applied to them. Modules [2,1,2,1,33,0,0][11] and [2,1,2,1,14,0,0][12] had the mask shown on the left in figure 43 applied to them. The greyscale [17] corresponds to different TDAC settings, black corresponding to TDAC-25 and white corresponding to TDAC+25. No effect on the number of noise hits was observed for these two modules. Almost all pixels on these two modules show no noise hits.

[6] offline ID [2,1,2,2,27,0,0], serial number 511818, geographical IDs D3A-S05-M5, D3A_B03_S2_M5
[7] offline ID [2,1,2,1,34,0,0], serial number 511476, geographical IDs D2A-S06-M3, D2A_B04_S1_M3
[8] offline ID [2,1,2,1,42,0,0], serial number 512746, geographical IDs D2A-S08-M1, D2A_B01_S1_M1
[9] offline ID [2,1,2,2,12,0,0], serial number 510392, geographical IDs D3A-S03-M1, D3A_B02_S2_M1
[10] offline ID [2,1,2,0,10,0,0], serial number 510418, geographical IDs D1A-S02-M3, D1A_B02_S1_M3
[11] offline ID [2,1,2,1,33,0,0], serial number 512351, geographical IDs D2A-S06-M5, D2A_B04_S1_M5
[12] offline ID [2,1,2,1,14,0,0], serial number 512831, geographical IDs D2A-S03-M2, D2A_B02_S2_M2

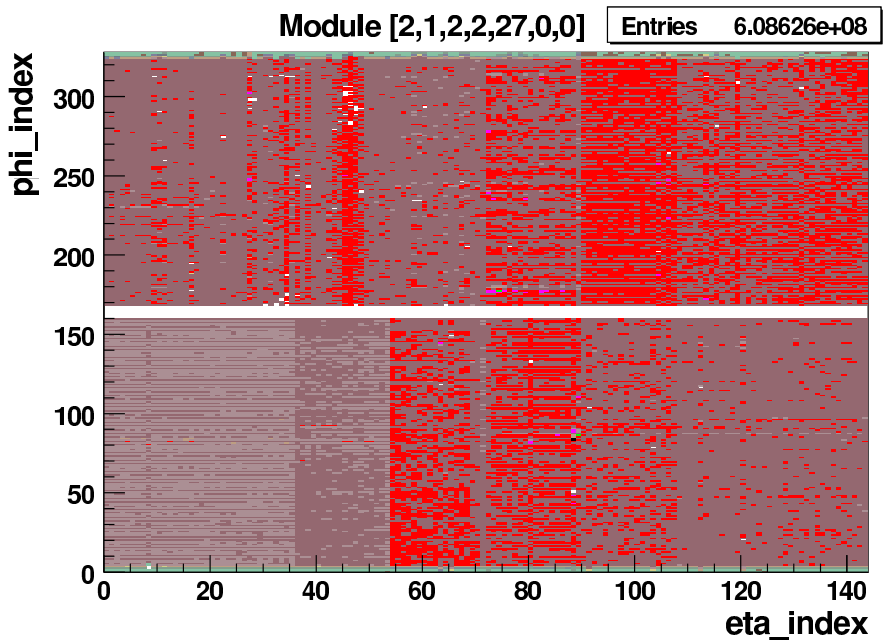


Figure 39: Hit map for module [2,1,2,2,27,0,0] which had a low threshold at TDAC-25 in run 1153.

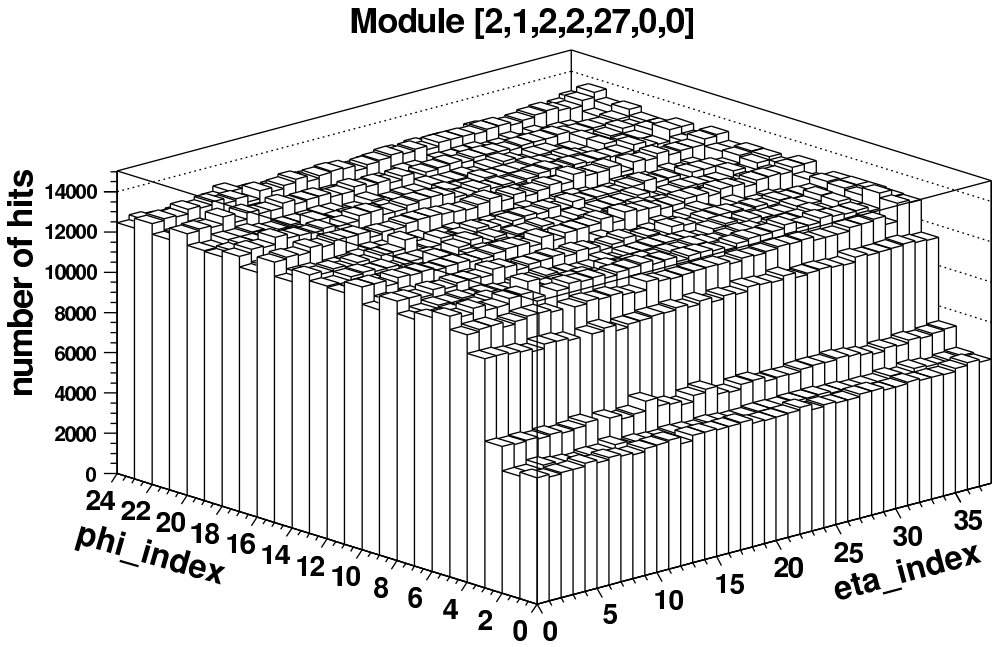


Figure 40: Hit map of a section of module [2,1,2,2,27,0,0] which had a low threshold at TDAC-25 in run 1153.

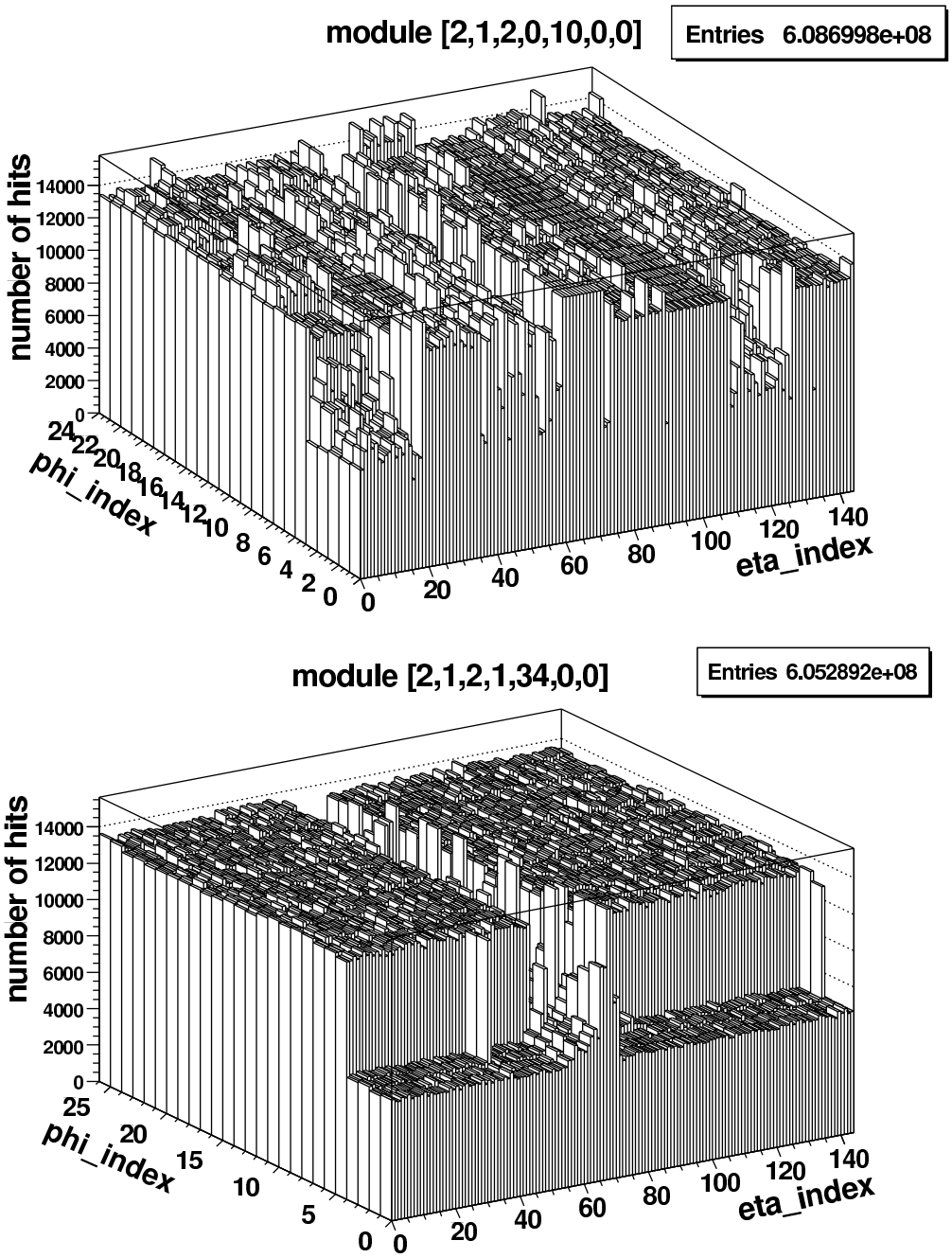


Figure 41: Hit maps of sections of two modules with unusually high noise levels in run 1144, in which all modules had a low threshold at TDAC-20.

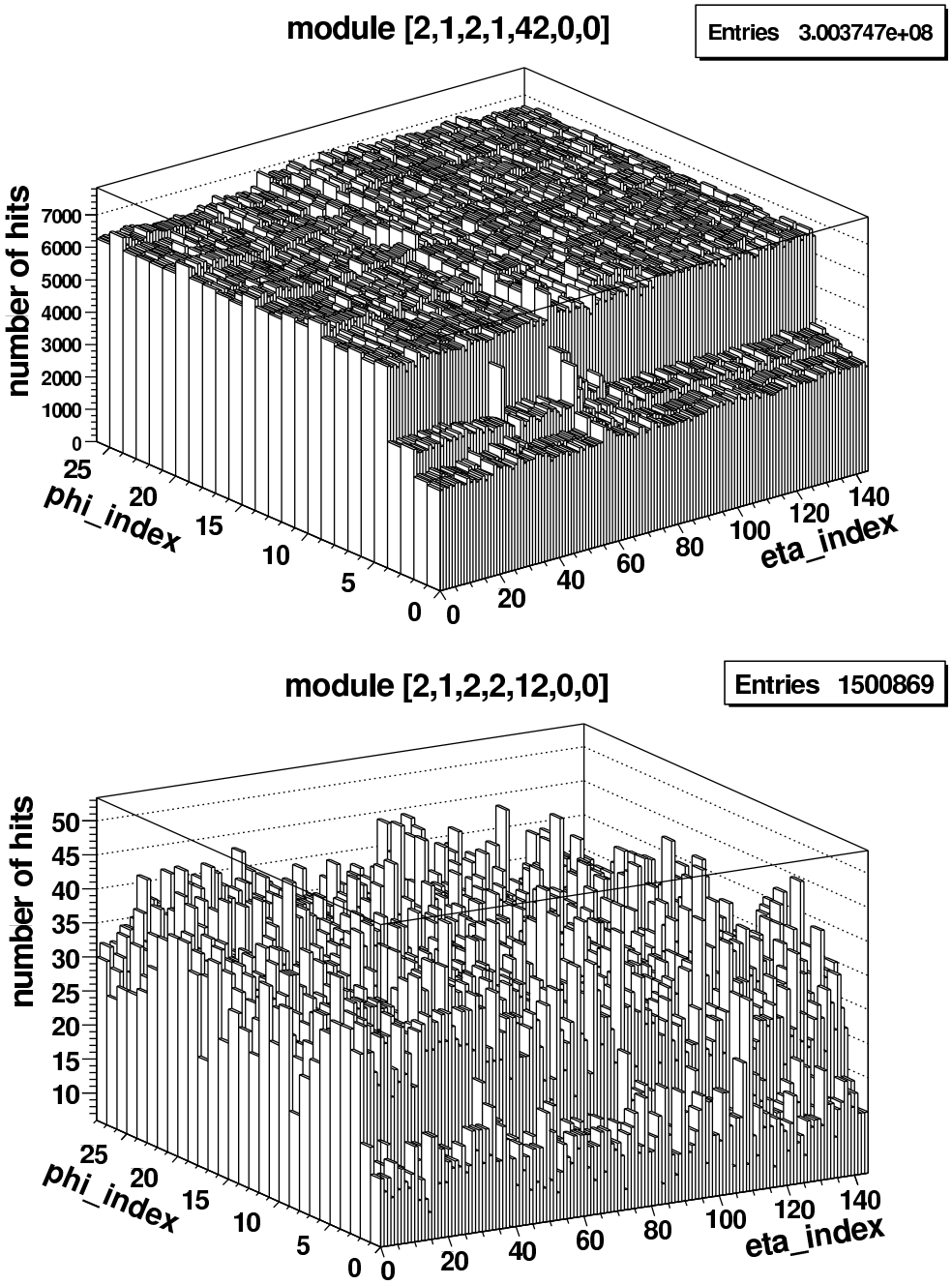


Figure 42: Hit maps of sections of two modules with unusually high noise levels in run 1144, in which all modules had a low threshold at TDAC-20.

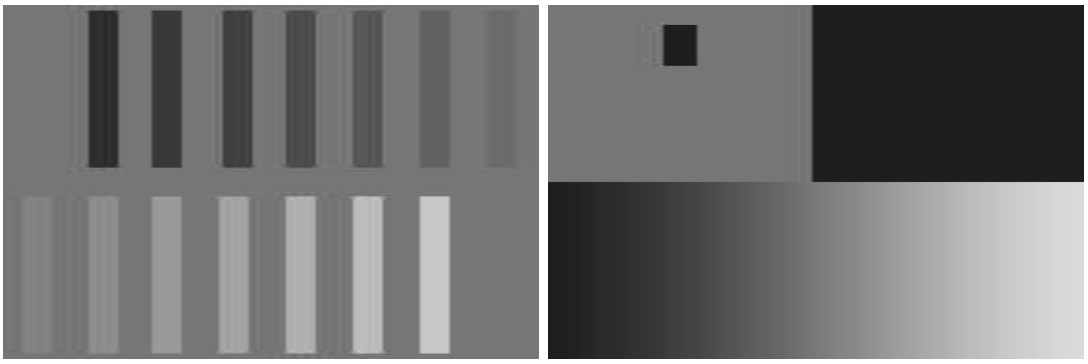

Figure 43: Greyscale images representing TDAC pattern masks that were applied to several modules in run 1153. Black corresponds to TDAC-25, white corresponds to TDAC+25. The mask on the left was applied to modules [2,1,2,1,33,0,0] and [2,1,2,1,14,0,0], the mask on the right was applied to modules [2,1,2,2,44,0,0] and [2,1,2,0,33,0,0].

The mask shown on the right in figure 43 was applied to modules [2,1,2,2,44,0,0][13)] and [2,1,2,0,33,0,0][14)]. Maps of the hits for these two modules are shown in figure 44. One can see an increased number of noise hits in the areas with the lowest thresholds, especially for the ganged pixels. Since the TDAC pattern mask was applied using column and row numbers instead of eta_indices and phi_indices the phi_index direction has to be flipped for module [2,1,2,0,33,0,0] for comparison with the greyscale image.

### 3.4 Summary

The noise in endcap A of the pixel detector was studied for several exemplary runs with different detector settings. The analysis of noise in the cosmics data run 1125 shows that the noise signal, as expected, is uncorrelated with the timing relative to the trigger signal and that the noise is dominated by *fixed pattern* noise, i.e. by hits in a relatively small number of noisy pixels. After removal of the noisy pixels the noise occupancy for the endcap is of the order $10^{-9}$. This result for the occupancy is confirmed in an analysis of the noise run 1131 in which a random trigger signal was used. A comparison shows that most of the noisy pixels in this run were found to be *special* during the production tests of the individual modules. An analysis of modules with a low threshold setting in runs 1153 and 1144 shows a moderate increase in the number of noise hits, especially in the ganged pixels. Several modules in these runs show an atypically high level of noise with the unexpected feature that the noise level in the first two to four rows of most front-end chips is only about half as high as in the other rows.

## 4 Cosmic Tracking Studies

The offline release used for the cosmic analysis is 12.3.0 including the latest fixes of the bytestreamer converter from InDetTB04ByteStream-00-00-52 and PixelIMap from InDetCabling-00-03-27. Pixel clusters were reconstructed using a simple clustering algorithm where all adjacent hits sharing at least one of sides were clustered together. The cluster position in the local x and y coordinators was computed using a charge weighted centroid with an uncertainty assigned as the pitch divided by $\sqrt{12}$. For cosmic tracking, we use the modified existing CTBSiTracking package [18]. First the algorithm loops over any pair of the pixel clusters from the inner and outer disk and linearly extrapolates to the middle disk. If there is a pixel cluster found within a search window of 1.5 mm in the middle disk, a cosmic track is reconstructed successfully. Then repeating the search to add overlap hits from the neighboring module. Finally, the best track is selected using SiCTBAmbSolver, which is based on the number of pixel clusters and the fitted chisq ($\chi^2 < 25$/ndof) in the x-z and y-z plane. The output track collection is saved as "SCT_Cosmic_Tracks" and there is no ESD or AOD written out, but CBNTs are saved that contain all

[13)] offline ID [2,1,2,2,44,0,0], serial number 510559, geographical IDs D3A-S08-M2, D3A_B01_S1_M2
[14)] offline ID [2,1,2,0,33,0,0], serial number 510963, geographical IDs D1A-S06-M5, D1A_B04_S1_M5

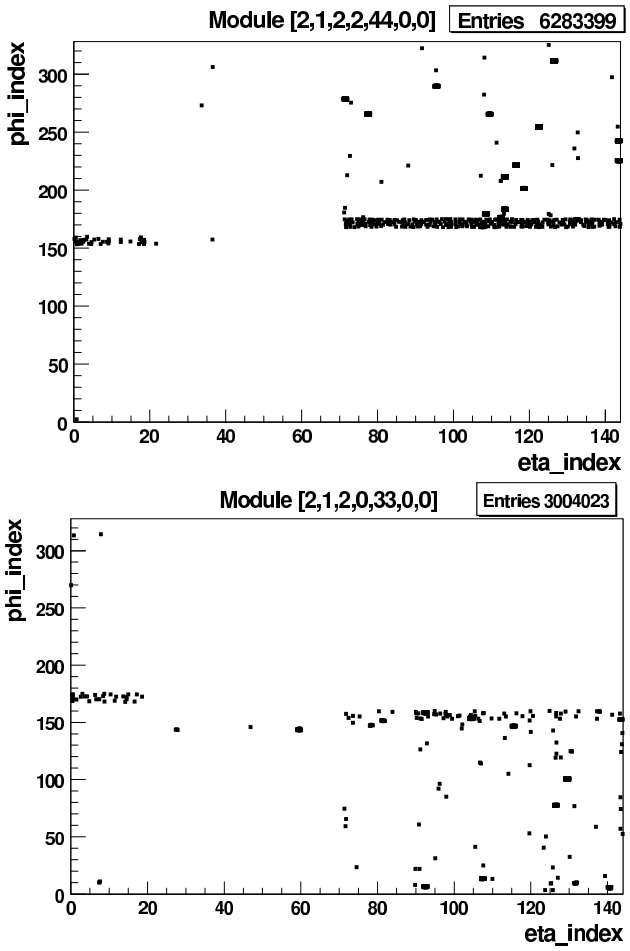


Figure 44: Hit maps for modules [2,1,2,2,44,0,0] and [2,1,2,0,33,0,0] in run 1153 to which the TDAC pattern mask corresponding to the greyscale image shown on the right in figure 43 was applied. Note that the TDAC pattern mask was applied using column and row numbers instead of eta_indices and phi_indices and hence the phi_index direction has to be flipped for module [2,1,2,0,33,0,0].

Table 3: The rate of cosmic tracks found in data and various Monte Carlo samples.

| Data Sample | Tracking Rate (%) | Overlap Fraction (%) |
|---|---|---|
| Data | $2.83 \pm 0.01$ | $23.4 \pm 0.2$ |
| Ideal MC | $\approx 6$ | $\approx 28$ |
| Realistic MC(disable modules) | $3.9 \pm 0.1$ | $24.6 \pm 0.9$ |

the information about pixels, clustering, and tracking for data analysis. Initially, there were couple problems found. For example, the channels of odd modules were in the wrong order, and the ganged pixels were not included properly. But they were quickly fixed after checking some basic quantities, like the minimum distance between the expected and the actual hits nearby shown in Figure 45 and the residuals between two overlap hits in adjacent modules shown in Figure 46 before and after the fix, respectively.

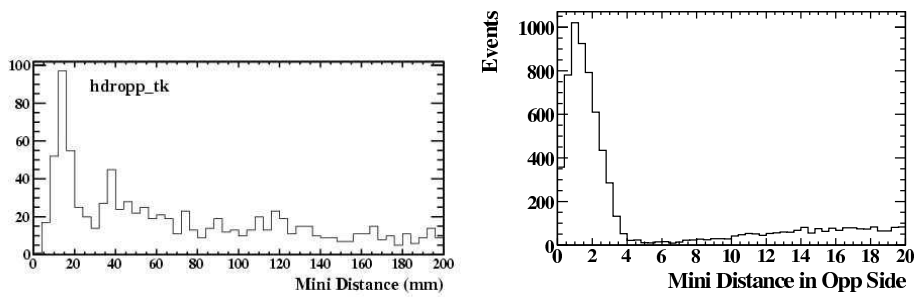


Figure 45: The minimum distance between the expected position and the nearby hits before (left) and after (right) fixing the readout order for the odd modules in the back of the disk.

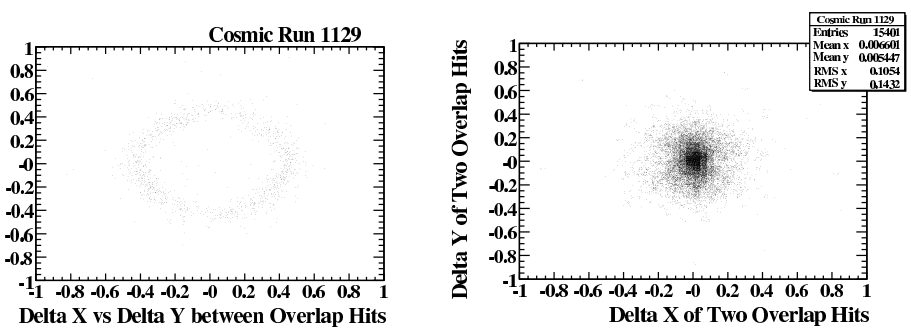


Figure 46: The scatter plot of dx and dy between the overlap hits before (left) and after (right) fixing the missing 8 ganged pixels in PixelIMap.

In order to better understand the detector performance, we have generated cosmic Monte Carlo with a realistic detector simulation that contains a list of modules that were disabled during the data taking. However, we still have not taken into account the special pixel map yet. So the simulation results are still optimistic comparing to the data.

Table 3 summaries the tracking rate per event and the fraction of tracks with overlap hits ($\geq 4$ pixel hits) in the data and the Monte Carlo with different conditions. The overall tracking rate is 2.83% in data, which is lower than realistic MC 3.9%. Howevre, the fraction of overlap hits are consistent between data and Monte Carlo, which indicates data and Monte Carlo have comparable pixel hit efficiencies.

Figure 47 shows the number of pixel clusters, total chisq, phi and theta of the reconstructed cosmic tracks. The agreement between data and Monte Carlo are quite good, except a spike in phi distribution caused by some noised modules in the data. We also checked the quality of clusters associated with the reconstructed track, which are shown in Figure 48 on the time over threshold (TOT or charge), the cluster

width, beam cross trigger identifier (BCID), and the module occupancy as function of phi +48*Layer where phi is the module number between 0 to 47 and Layer is the disk number between 0 to 2. A nice Landau peak is clearly visible. However, the TOT is somewhat shifted to higher side compared to the Monte Carlo prediction that was tuned based on the test beam data. This is not understood yet. Two noise modules were clearly visible in Layer 1 and Layer 2, which causes a spike in the phi distribution of reconstructed tracks.

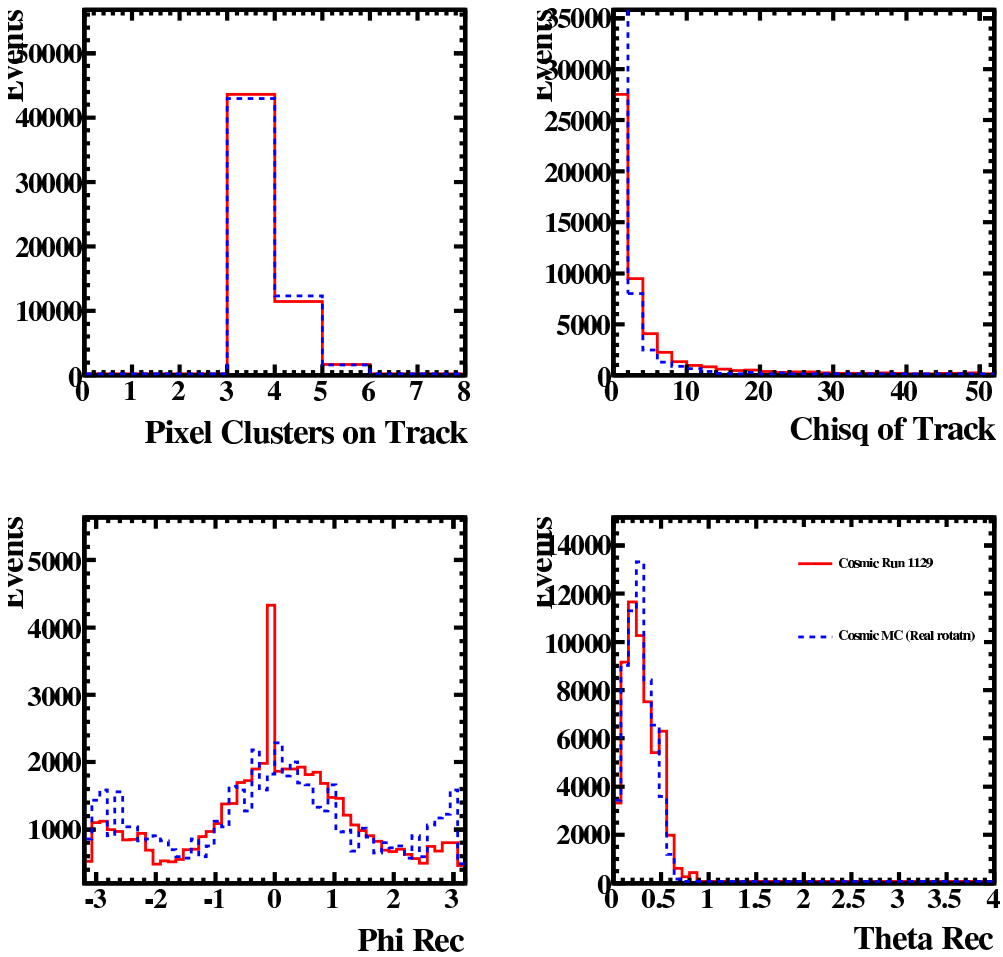


Figure 47: The comparisons of cosmic tracking in terms of the number of pixel hits (top left), the chisq of fit (top right), the phi and theta of the reconstructed cosmic tracks (bottom left and right ). The solid curve is data and the dashed one is Monte Carlo.

## 5 Alignment with Overlap Residuals

There are about 24% of tracks containing an overlap hits from neighboring modules, which can be used to check the relative alignment between adjacent modules. Before doing so, we need to make sure the noise contamination of overlap hits are small, as shown in Figure 49 for the overlap hits in terms of the module occupancy, xy scatter plot, track phi and a scatter plot of TOT vs the fitted track chisq. As expected, the tracks with overlap hits seem much more reasonable, and pure compared with the Monte Carlo.

Assuming the module as a rigid body, there are 4 parameters to describe the module position inside the disk:

- Shift $X_0$ in local X axis along the short pixel direction

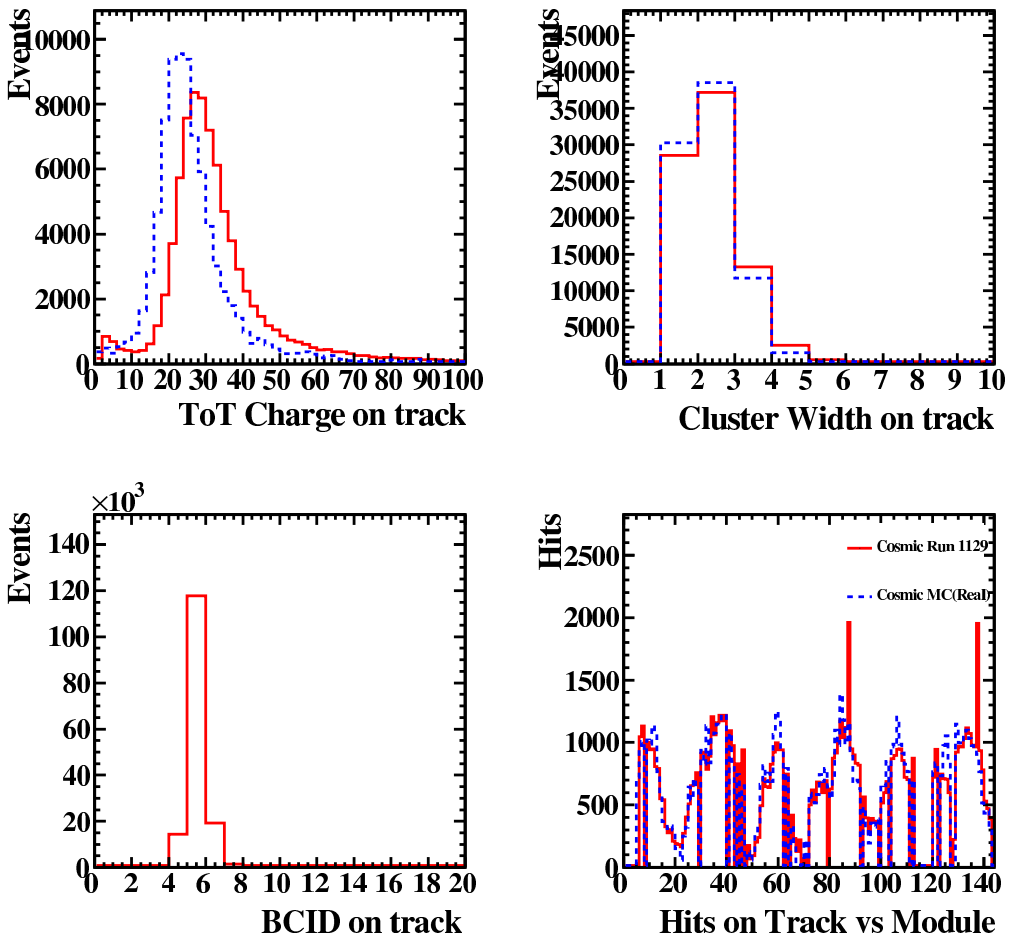


Figure 48: The comparisons of cosmic tracking in terms of the TOT (top left), the cluster width(top right), the beam crossing (BCID) and the module occupancy (bottom left and right ). The solid curve is data and the dashed one is Monte Carlo.

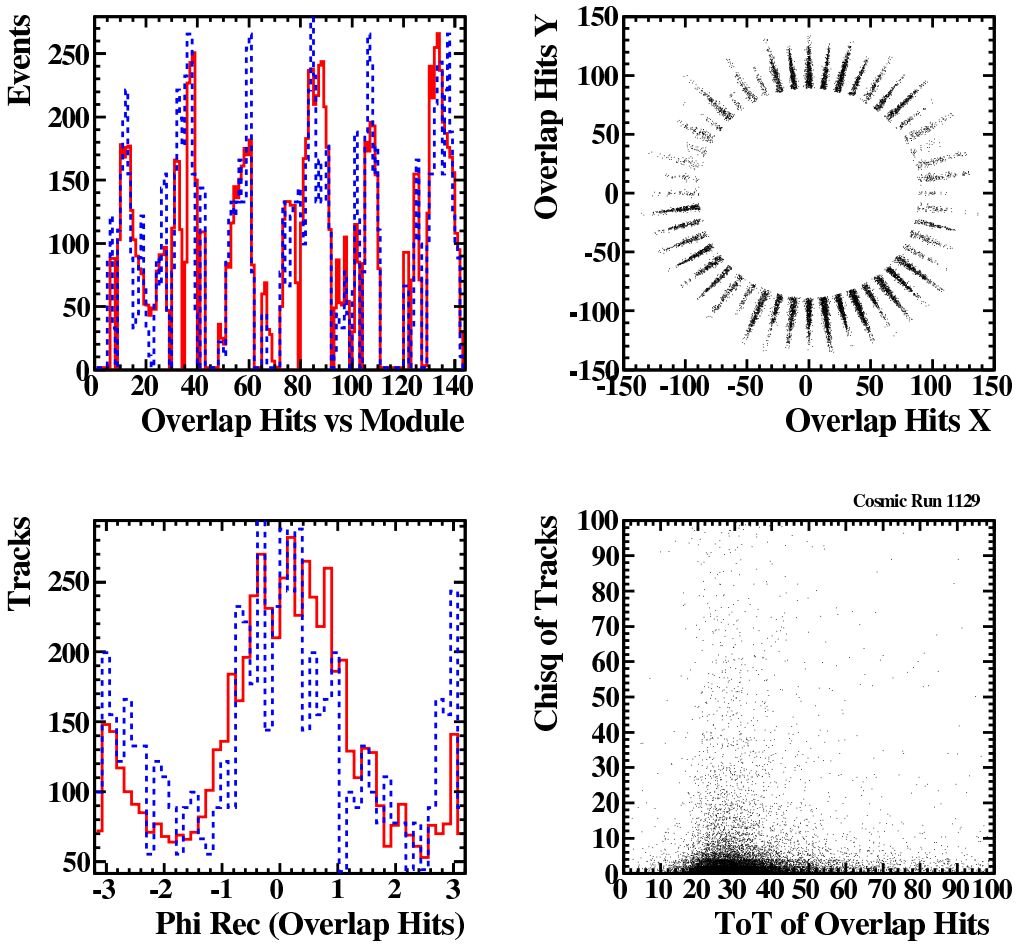


Figure 49: The distributions of the overlap hits in terms of the module occupancy (top left), xy scatter plot (top right), track phi (bottom left) and a scatter plot of TOT vs the fitted track chisq (bottom right). The solid is for the data and the dash is for the Monte Carlo.

- Shift $Y_0$ in local Y axis along the long pixel direction
- Shift $Z_0$ in local Z axis perpendicular to the disk
- Rotation $\alpha_0$ along local Z axis

The relative alignment constants were determined considering the difference $\Delta x$ and $\Delta y$ between the positions of the overlap hits in the local reference plane of the odd module after taking into account the track extrapolation. Figure 50 shows the overlap residuals vs the number of odd modules in the left and right overlap regions. The $dX_0$ and rotation $d\alpha_0$ were determined by a line fit of $\Delta x$ vs local Y of the hit in the odd module. The $dY_0$ were determined from the mean of $\Delta y$. The $dZ_0$ were determined by a line fit of $\Delta x$ vs $tan\theta \cdot cos\phi$ where $\theta$ and $\phi$ are the angles of the reconstructed cosmic track. The overall residuals before and after alignment correction are shown in Figure 51 with a nominal geometry with $dz = 4.25$ mm,instead of 4.2 mm. The resolution in LocX improves from 21.2 to 17.8 $\mu m$ while the resolution in LocY remains the same at 160 $\mu m$. Figure 52 summarizes the relative alignment constants as a function of odd modules in the left and right overlaps regions. Most of them are within 20 $\mu m$, which indicates the pixel endcapA is well reconstructed.

We have also checked the residuals with the endcapA as built survey geometry [20], which has slighter better resolution of 20.7 $\mu m$ than the one with nominal geometry. In order to check the correlation between the alignment constants and the survey data, we select the modules with more than 50 overlap hits and compare the relative alignment constants as shown in Figure 53, which seems indicate some correlations do exist between the alignment and survey, but not as strong as we hoped. Another interesting test is to check the relative alignment between modules in both front and back adjacent modules in the same sector or different sectors since the survey is conducted much more accurate for the front modules in the same sector than the back modules or modules in cross different sectors. Figure 54 shows the comparison between the alignment and the survey data. Again, they seem correlated in some degree. At this moment, it would be difficulty to derive absolute alignment constants for the modules within the disk since some of modules were not function during the cosmic data taken. However, the results are quite impressive for what we have achieved so far with such limited data. Some of difficulties are due to limited data statistic or some of unknown systematic which we have not uncovered yet.

# 6 Lesson learned and future improvements

In the previous sections there have been presented a wide spectrum set of studies that provides significant insight about what to expect when the full detector will be in operation.

First of all, from the noise measurements, it is possible to conclude that the most relevant noise source is *fixed pattern noise*, which in principle can be suppressed almost completely by masking, either on-line or off-line the noisy channels.

Almost the totality of noisy channels was detected as problematic during the module acceptance tests. Unfortunately, it is not possible, by the simple fact a pixels was *special* during these tests, to predict this specific pixel will be noisy. Therefore the number of *special* pixels can be taken as an upper limit to the inefficiencies, including both dead channels and channels masked because of the excessive noise rate. This number is few per mill of the total number of pixels.

Random noise, instead, is at a very low level and can be neglected for most application.

Digitization parameters have been taken from the characterization tests performed during module production. The simulation produced with these parameters has been compared with the collected data. This proved to be a good validation of the ATLAS pixel detector simulation and makes us confident that, extraction of calibration data on-site, from dedicated runs, will be a reliable source of updated information about the evolution of the detector operating conditions in the LHC running.

The tracking studies, especially the ones related to particles passing in the overlap regions between adjacent modules, have been very useful in spotting problems in our geometry description. In particular, different conventions in the detector description and Reconstruction software have been spotted and properly taken into account. Another observation was that a mismatch between the fabrication drawing and the actual detector assembly, initially observed in the sectors' survey, is confirmed by alignment

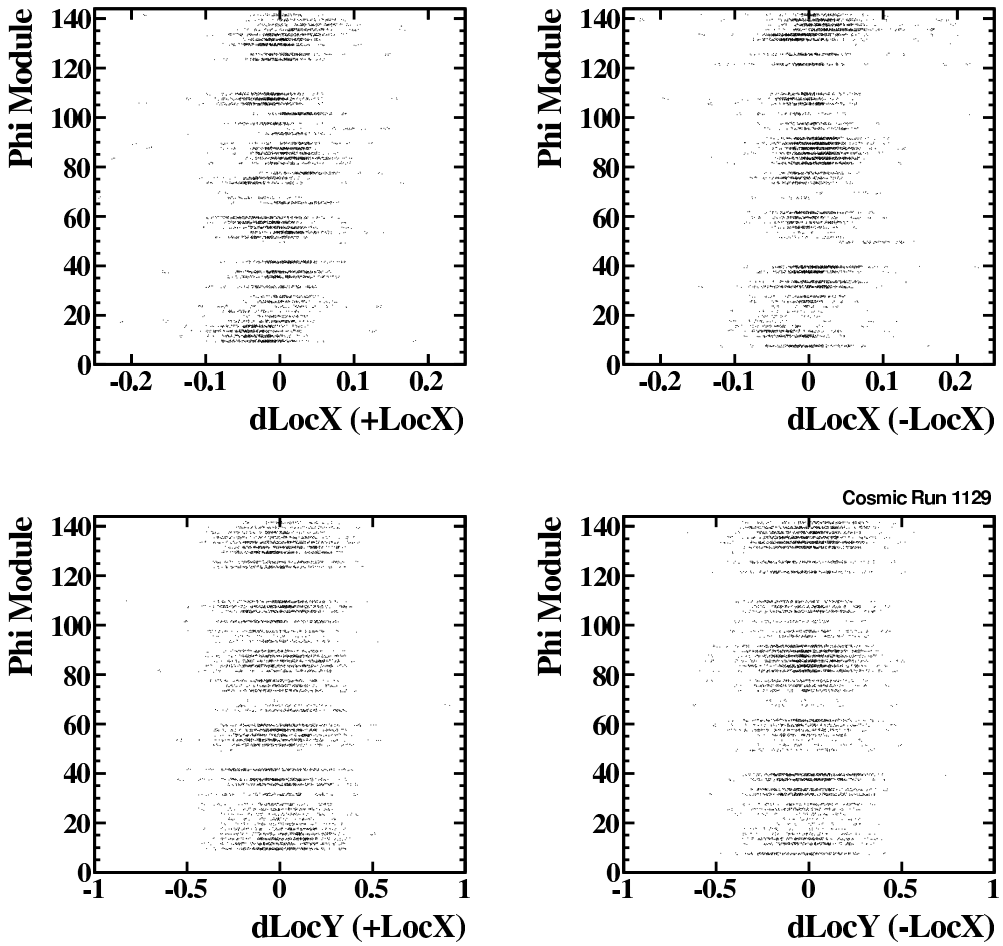


Figure 50: The overlap residual distributions as function of module number (module+48*Layer): residual X in +LocX and -LocX of odd modules (top) and residual Y (bottom).

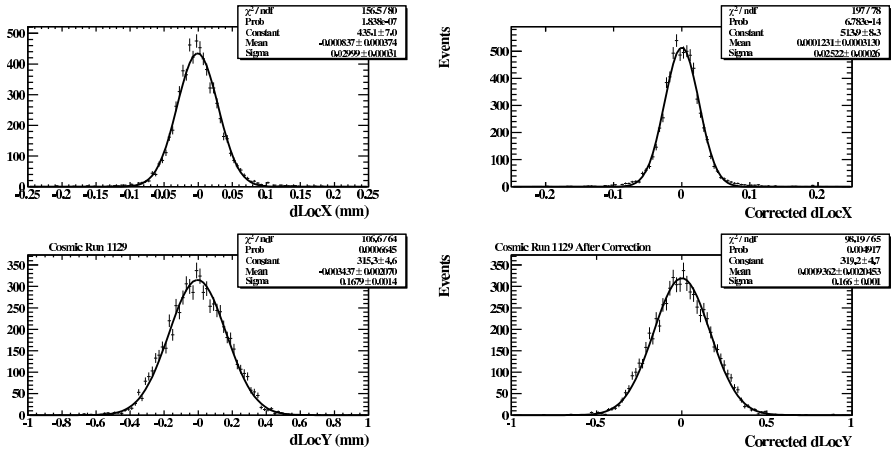


Figure 51: The overlap residual in LocX and LocY with nominal geometry with dz=4.25 mm (left) and after alignment correction (right).

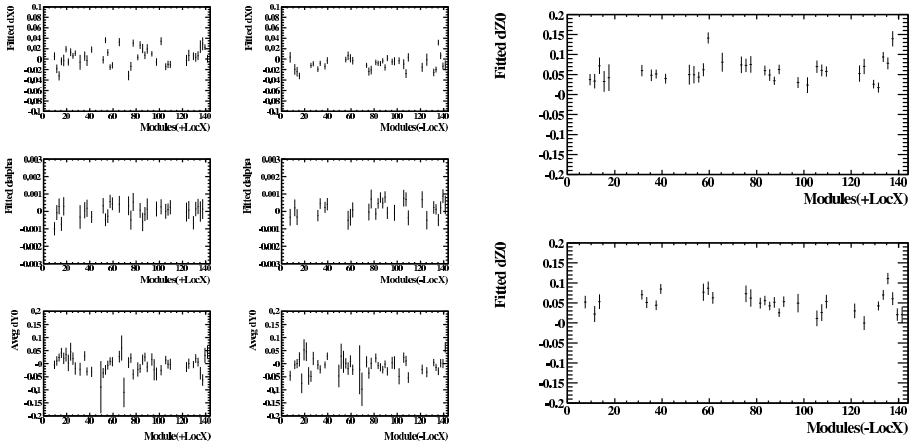


Figure 52: The relative alignment constants ($dX_0$, $dY_0$, $d\alpha_0$ and $dZ_0$ ) derived from the cosmic data as function of odd module in the overlap region with +LocX and -LocX.

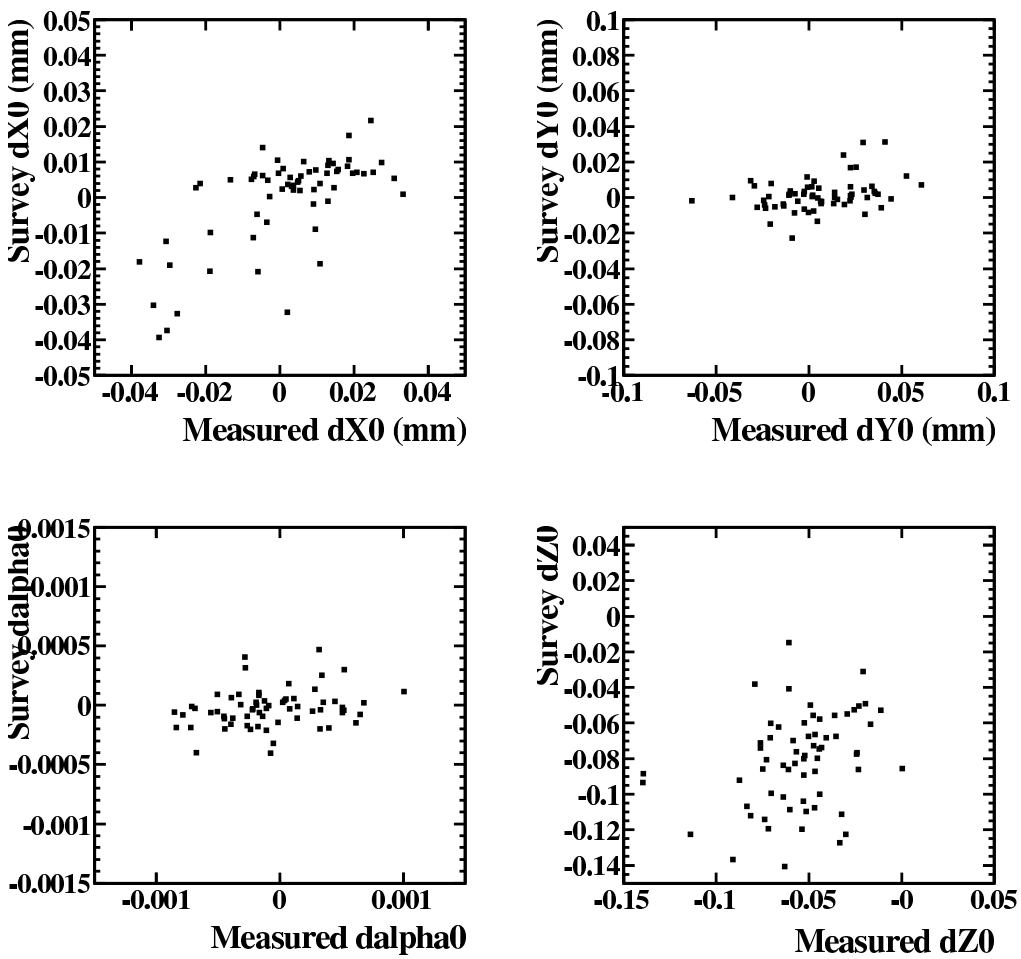


Figure 53: The scatter plot between the measured relative alignment and survey for neighboring modules.

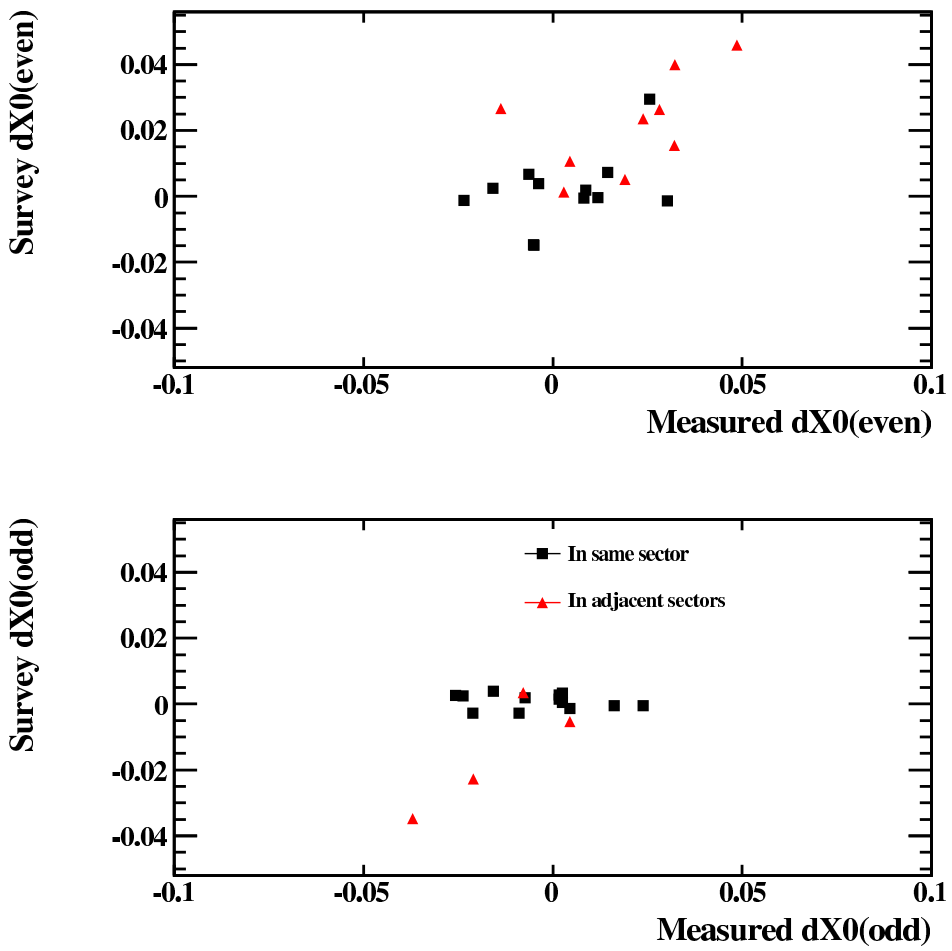


Figure 54: The scatter plot of relative alignment and survey between neighboring modules in the front disk or even modules (top) and in the back disk or odd modules (bottom). The back point is for modules in the same sector and the triangle point is for modules in different sectors.

data. The better agreement of alignment data with the survey than with the nominal drawings, show the survey is a reliable starting point.

This will be of much more relevance for the barrel part, since in that region the disagreement between the survey and nominal position is much worse, at the 200 $\mu$m level.

Besides the analysis summarized above this run was a very useful opportunity to finalize many software updates needed for the detector commissioning, in particular a complete revision of the digitization, the implementation of a calibration database in COOL, which can be accessed both by simulation and reconstruction processes, and finally the insertion of the survey information to be used as initial alignment step. The technical aspects of this updates in the pixel software and description are described in an accompanying Computing System Commissioning note [19].

There are some additional studies interesting for the pixel offline analysis and calibration, which were not completed in time to be inserted in this note but for which the analysis is going on.

These include the collection of DCS information, in order to estimate the amount of data that will be collected during normal data taking and smoothing parameters for the PVSS logging and transfer to COOL.

Another ongoing study is the check of the timing using the LVL1 distribution of the modules and comparing it with the simulation, in order to develop an algorithm for synchronization of the pixel detector.

# 7 Conclusion

This document summarizes the results of the offline analysis for the pixel endcapA system test cosmic data. The setup consists of one pixel endcap of three disks, for a total of 144 modules and 6.6 million channels, about the 8% of the full detector. The endcap is hung vertically and sandwiched between one scintillator at the top and a set of three scintillators at the bottom for trigger. It is completely equipped with services and managed by a initial production of the ATLAS DAQ system components with the goal of exercising the readout system, data taking and testing the offline reconstruction chain.

Runs with random trigger allow us to measure the noise rate. The observed noise occupancy is achieved to $10^{-9}$ after removing the noisy pixels. Comparison with the detector characterization performed during the detector assembly shows that most of these noisy pixels were already flagged during the production test.

The tracking studies, especially the ones related to particles passing in the overlap regions between adjacent modules, have been very useful in spotting problems in our geometry description and can be used for the relative alignment between the adjacent modules. When using the geometry taken from the detector survey, an initial resolution of 21.2 $\mu m$ is obtained. After a preliminary alignment this improves to 17.8 $\mu m$. The difference with the 15.8 $\mu m$ expected from MC simulation are probably due to residual alignment uncertainties which are under investigation.

The experience gained in the SR1 running will be also extremely useful for the preparation of the cosmics running within the whole ATLAS setup in the pit and its analysis and understanding.

# References


[1] M. Keil *et al.*, *Pixel Endcap A System Test*, in preparation.

[2] M. Leyton *et al. Service Tests for the ATLAS Pixel Detector*, ATL-IP-QA-0026 (2007).

[3] G. Alimonti *et al.*, *Analysis of testbeam data of ATLAS Pixel detector modules with a high intensity pion beam*, ATL-COM-INDET-2005-012, (2005).

[4] M. Zdražil *et al.*, *Pixel EndCap A cosmic test documentation on A TLAS Twiki pages*, https://twiki.cern.ch/twiki/bin/view/Atlas/PixelCosmic.

[5] M. Keil, P. Morettini *et al.*, *Pixel Detector System Test - ATLAS TWi ki pages*, https://twiki.cern.ch/twiki/bin/view/Atlas/SystemTest.

[6] K. Einsweiler *et al.*, *ATLAS On-detector Electronics Architecture*, v ersion 3.0, Dec 9, 2003. Also see Kevin's presentation at LBNL Instrumentation Colloquium, April 13, 200 5, *The Atlas Pixel Detector*, p. 8-18 mainly.

[7] K. Einsweiler *et al.*, *ATLAS On-detector Electronics Architecture*, v ersion 3.0, Dec 9, 2003. Also see Kevin's presentation at LBNL Instrumentation Colloquium, April 13, 200 5, *The Atlas Pixel Detector*, p. 8-18 mainly.

[8] S. Golfarb and A. Schaffer *et al.*, *Definition of Off-line Readout Id entifiers for the ATLAS Detector*, ATL-SOFT-2001-004, (2001).

[9] SuDong, H. Gray *et al.*, *Pixel Scintillator Trigger Layout documentat ion - ATLAS TWiki pages*, https://twiki.cern.ch/twiki/bin/view/Atlas/PixelScintillatorTriggerLayout.

[10] S. Eidelman *et al.*, *Review of Particle Physics*, Physics Letters _f B 592, 1 (2004). See http://pdg.lbl.gov for Particle Listings and complete reviews, plus a direc tory of online HEP information.

[11] A. di Simone *et al.*, *Cosmic simulation package documentation on ATLA S TWiki pages*, https://twiki.cern.ch/twiki/bin/view/Atlas/CosmicSimulation.

[12] D. Costanzo, G. Gorfine, *PixelGeoModel package documentation on ATLAS TWik i pages*, https://twiki.cern.ch/twiki/bin/view/Atlas/PixelGeoModel.

[13] M. Gallas and Simone Dell'Acqua *et al*, *GEANT4 ATLAS detector simulat ion applications*, http://atlas-computing.web.cern.ch/atlas-computing/packages/simulation/geant4/G 4Atlas-Apps/doc/index.html.

[14] O. Oye *et al.*, *InDetCosmicSimAlgs simulation package documentation on ATLAS TWiki pages*, https://twiki.cern.ch/twiki/bin/view/Atlas/InDetCosmicSimAlgs.

[15] M. Elsing, F. Tegenfeldt *et al.*, *ATLAS Pixel Detector digitization package on ATLAS TWiki pages*, https://twiki.cern.ch/twiki/bin/view/Atlas/PixelDigitization.

[16] M. Zdražil *et al.*, *How to run simulation of pixel endcap A cosmic test*, https://twiki.cern.ch/twiki/bin/view/Atlas/HowToRunPixelEndCapCCosmicSimulation.

[17] D. Dobos, J. Weingarten, private communication.

[18] T. Cornelissen, *CTBtracking: track reconstruction for the testbeam and cosmics*, ATL-INDET-INT-2006-001 (2006).

[19] *Pixel Software Commissioning*, in preparation

[20] A. Andreazza, V. Kostyukhin, R. Madaras, *Pixel Survey*, ATL-IP-QC-0035 (in preparation).